Engineering Fracture Mechanics 322 (2025) 111123

Contents lists available at ScienceDirect

Engineering Fracture Mechanics

journal homepage: www.elsevier.com/locate/engfracmech

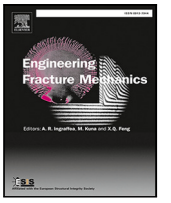

Rupture directivity and poroelastic coupling in earthquakes induced by fluid injection

Sandro Andrés [a,*], David Santillán [a], Juan Carlos Mosquera [b], Luis Cueto-Felgueroso [a]

[a] Department of Civil Engineering: Hydraulics, Energy and Environment, Universidad Politécnica de Madrid, Madrid, 28040, Madrid, Spain
[b] Department of Continuum Mechanics and Structures, Universidad Politécnica de Madrid, Madrid, 28040, Madrid, Spain

ARTICLE INFO

Keywords:
Induced seismicity
Rupture directivity
Undrained response
Poroelasticity

ABSTRACT

Earthquakes induced by the human-made injection or extraction of fluids have recently become a major concern in energy technologies. When frictional and hydromechanical conditions lead to fault reactivation, unstable slip can occur and rupture propagates across the fault with a pattern analogous to two crack tips, spreading away from the hypocenter. During the earthquake the rupture tips can propagate symmetrically or along a preferred direction. These propagation patterns are related with the effects of the earthquake, and are essential due to the predominance of almost-unilateral ruptures in large earthquakes catalogs.

We study how poroelastic coupling controls the directivity of the rupture in earthquakes induced by pore pressure changes. The directivity patterns observed in earthquakes ruptures may be explained by a contrast in material properties across the fault as previous studies have shown. Here we show that rupture asymmetries may be also promoted by the pressure and stress changes induced by fluid injection prior to rupture, together with the undrained pressure response during coseismic slip. We employ fully coupled hydromechanical simulations of poroelastic media with rate-and-state faults, and analytical solutions to perform a dimensionless analysis. We observe that, depending on the flow conditions and the initial fault stress state, directivity patterns range from almost-symmetric to almost-unilateral.

We explain the rupture directivity pattern in terms of the conditions of fault confinement and pore pressure diffusion, and identify two mechanisms that control the symmetry of the earthquake rupture. Firstly, the pore pressure distribution prior to earthquake, which depends on the distance between the injection well and the fault, controls the heterogeneity of fault strength along the fault. Secondly, the undrained effect due to coseismic fault slip, which is directly related to the initial confinement, causes an increase or decrease of pore pressure on either side of the fault.

Our results contribute to understand the impact of poroelasticity on rupture directivity in injection-induced earthquakes and offer a feasible explanation of almost-unilateral rupture patterns.

* Corresponding author.
E-mail address: sandro.andres@upm.es (S. Andrés).

https://doi.org/10.1016/j.engfracmech.2025.111123
Received 3 October 2024; Received in revised form 14 March 2025; Accepted 5 April 2025
Available online 18 April 2025

Nomenclature

a	direct effect parameter
a_l	left front advance distance
a_r	right front advance distance
b	friction evolution parameter
d	injection well-fault distance
d_{95}	width of the pressure bell at reactivation
d_F	fault thickness
D	rupture directivity ratio
D_c	characteristic slip length
$\mathcal{D}$	hydraulic diffusivity
E	Young modulus
E_1	exponential integral function
$\mathbf{g}$	gravity vector
G	shear modulus
$\mathbf{I}$	identity tensor
k	intrinsic permeability
k_F	fault permeability
K	bulk modulus
l	longitudinal coordinate along the fault
L_b	Dieterich nucleation length scale
p	pore pressure
p_{crit}	critical pressure required for fault reactivation
p_F	fault pore pressure
p_+	pressure at fault south side
p_-	pressure at fault north side
p_{max}	maximum pressure of both sides
q	injection flow rate per unit length
r	distance to injection point in Theis' solution
S	storage coefficient
S_F	fault storage coefficient
$\mathbf{u}$	displacement field
t	time
t_d	diffusion time
t_r	fault reactivation time
$T_{n,F}$	total normal stress
U	proportion unilateral rupture
v_0	model input flow velocity
V	fault slip velocity
V_0	slip reference velocity
α	ratio between advance distances of rupture fronts
α_B	Biot coefficient
$\alpha_{B,F}$	fault Biot coefficient
β	fault orientation angle
$\boldsymbol{\varepsilon}$	strain tensor
ε_v	volumetric strain
η_f	fluid viscosity
θ	friction state variable
λ	first Lamé parameter
μ	friction coefficient
μ_0	steady-state friction coefficient
ν	Poisson ratio
$\pi_{1,2,3,4}$	dimensional analysis parameters

ρ_b	saturated density of bulk rock
ρ_f	fluid density
$\boldsymbol{\sigma}$	stress tensor
$\boldsymbol{\sigma}'$	effective stress tensor
σ'_F	effective normal stress
σ_0	initial normal stress
σ_x	stress along x-axis
σ_y	stress along y-axis
τ	shear stress
τ_0	initial shear stress
τ^*	frictional strength
ϕ	porosity
χ_s	solid compressibility
χ_f	fluid compressibility
$\partial\Omega_F$	fault-matrix interface

1. Introduction

Induced seismicity has recently raised societal concern and has become a major concern in energy technologies [1]. A paradigmatic case is the vast increase in frequency and intensity of earthquakes in central and eastern United States [2,3], yet other episodes are given in Central Europe [4–6], western Canada [7], China [8], and other locations across the globe [9]. These earthquakes are often linked with the energy industry, for instance, the disposal of wastewater from oil and gas recovery into deep formations [10–13], hydraulic fracturing [14–18], enhanced geothermal systems [5,19,20], CO_2 sequestration into deep saline formations [21,22], or even the creation of new water reservoirs [23]. Most induced earthquakes have magnitudes lower than 3.6, which is too small to cause serious risks [2], although magnitudes up to $Mw = 5.7$ have been reported, for instance, the 2011 event in Prague, Oklahoma, USA, that was induced by waste-water injection [12,24]. Therefore, estimates of the induced ground motion and earthquake magnitude have become a central issue [25].

The rupture propagation has important consequences in terms of potential damages and seismic hazard [26]. In this sense, the strength of the ground motion is affected by the rupture process, particularly by its directivity [27]. Rupture directivity is the existence of a predominant direction of propagation, i.e., earthquake ruptures may be bilateral or unilateral. According to [28], a perfect bilateral rupture produces two equal-velocity rupture fronts that propagate in opposite directions, whereas a perfect unilateral rupture results in a single rupture front. The direction of the rupture propagation affects the pattern of fault slip produced by the earthquake [29]. The strength of the ground motion will be greater for unilateral ruptures, as they concentrate a single zone of amplified slip. Unilateral ruptures seem to prevail in large earthquakes, both natural or induced [30–34]. In the case of small natural events ($2 \leq M \leq 5$), evidence for bilateral rupture character has been found [32,33], as well as in induced microseismic events ($M \leq 2$) [35]. Directivity causes polarization in approximately fault-normal orientations, i.e., involves large pulses of motion to be oriented in the direction perpendicular to the fault, causing the strike-normal ground motions to be larger than the strike-parallel ground motions at periods longer than 0.5 s. The conditions to generate forward rupture directivity effects are easily met in strike-slip faulting [36].

Understanding the rupture process, particularly rupture directivity, is crucial to assessing future earthquake risks. The rupture process depends on many factors of the fault and the host rock. The presence of fault heterogeneity, such as barriers or asperities, partially controls the direction of the rupture propagation [37]. The contrast in elastic and poroelastic material properties on both sides of faults may induce asymmetric ruptures on faults governed by slip-weakening friction [38–41], rate-and-state friction [42,43], or even on faults with constant friction coefficients due to the existence of a generalized Rayleigh wave [44]. Nevertheless, observations and numerical simulations demonstrated that rupture directivity is unlikely to be predictable based on the material contrast [45]. Therefore, other factors may control the rupture propagation direction.

Here we analyze the impact of 1) the rock confinement and 2) the distance between the injection point and the fault on rupture directivity. We simulate the host rock as a poroelastic material and the fault as a contact surface with friction governed by a rate-and-state law. We focus on the initial stress state on the fault at the onset of the slip and the undrained response during the rupture process. We link the rupture directivity to the poroelastic response and the initial stress state at the onset of the slip which, in turn, both depend on the rock confinement and the distance between the injection point and the fault.

Our paper is organized as follows: in Section 2 we describe the mathematical formulation of our model. We present our model set-up to study the rupture directivity in Section 3. In Section 4 we describe and discuss the modeling results. Lastly, we present the conclusions of our work in Section 5.

2. Methodology. Mathematical model

In this section, we describe our mathematical model to simulate the nucleation and rupture of injection-induced earthquakes. We simulate the host rock as a poroelastic material [46,47] and the fault as a contact surface with friction governed by a rate-and

state-friction model [48,49]. This mathematical model allows us to explore the impact of the initial stress field in the host rock and the distance between the injection well and the fault on the rupture directivity.

2.1. Hydromechanical model

We simulate the host rock as a poroelastic material. We adopt the classical theory of linear poroelasticity [46,47] and we solve the coupled evolution of fluid pressure, rock deformation, and frictional contact on the fault [50,51]. The standard quasi-static form of Biot equations for single-phase flow reads as follows:

$$S\frac{\partial p}{\partial t} + \alpha_B \frac{\partial \varepsilon_v}{\partial t} - \nabla \cdot \left(\frac{k}{\eta_f} \left(\nabla p - \rho_f \mathbf{g} \right) \right) = 0, \tag{1}$$

$$\nabla \cdot \boldsymbol{\sigma} + \rho_b \mathbf{g} = \mathbf{0}, \tag{2}$$

where α_B is the Biot coefficient, S is the storage coefficient, $\varepsilon_v = \mathrm{tr}(\boldsymbol{\varepsilon})$ is the volumetric strain, $\boldsymbol{\varepsilon}$ is the strain tensor, p is the pressure field, k is the intrinsic permeability of the porous medium, η_f is the fluid dynamic viscosity, ρ_f is the fluid density, ρ_b is the saturated density of the bulk rock, $\mathbf{g}$ is the vector of gravity accelerations, and $\boldsymbol{\sigma}$ is the total stress tensor. The storage coefficient S depends on the rock porosity ϕ and the fluid and matrix compressibilities χ_f and χ_s as follows:

$$S = \phi\chi_f + (\alpha_B - \phi)\chi_s, \tag{3}$$

where $\chi_s = (1 - \alpha_B)/K$ and K is the bulk modulus of the rock.

We assume that the host rock is a linear poroelastic material that undergoes small deformations under plane strain conditions. Hence, the effective stress tensor $\boldsymbol{\sigma}'$ is a linear function of strain tensor $\boldsymbol{\varepsilon}$ as follows:

$$\boldsymbol{\sigma}' = \boldsymbol{\sigma} + \alpha_B p\mathbf{I} = 2G\boldsymbol{\varepsilon} + \lambda \mathrm{tr}(\boldsymbol{\varepsilon})\mathbf{I}, \tag{4}$$

$$\boldsymbol{\varepsilon} = \frac{1}{2}\left(\nabla \mathbf{u} + \nabla \mathbf{u}^T \right), \tag{5}$$

where λ and G stand for the Lamé constants, and $\mathbf{u}$ is the displacement field. With the chosen sign criterion, tensile stresses are positive.

We opt for a quasi-static model to reduce the computational cost of the simulations. The phases of earthquakes before rupture, fault reactivation, and earthquake nucleation are slow phenomena where dynamic effects can be neglected. During the rupture phase of earthquakes, although the propagation of seismic waves can compress or tension both the fault and the host rock, the effects of waves on the pore pressure are less relevant than those produced by the undrained response caused by the sudden deformation of the areas around the fracture tips [52]. In Appendix B we include a comparison between quasi-static and dynamic approaches to show that there are small differences in the rupture propagation symmetry.

2.2. Flow along and across faults

We model the flow along and across the fault. Our model simulates the flow within the fault with a lower-dimensional model. We assume that the fault is a thin poroelastic medium with thickness d_F and we impose that the displacements and pore pressure on the fault wall are equal to that of the host rock at the matrix–fault interface. In the following formulation, the subscript F denotes fault parameters, the subscript + denotes the host rock parameters at one matrix–fault interface, and − at the opposite matrix–fault interface. Hence, the volumetric strain of the fault wall is equal to that of the host rock at the interface, *i.e.* $\varepsilon_{v,F} = \varepsilon_{v,\pm}$ [20,53]. The mass conservation for the fluid along the fault reads:

$$d_F \frac{\partial (S_F p_F + \alpha_{B,F}\varepsilon_{v,F})}{\partial t} - \nabla_l \cdot \left(d_F \frac{k_F}{\eta_f} \nabla_l \left(p_F - \rho_f \mathbf{g} \right) \right) = 0, \tag{6}$$

where l is the longitudinal coordinate along the fault and k_F is the longitudinal fault permeability. We impose pressure continuity between the fault and the host rock at one of the matrix–fault interface, as follows:

$$p_F = p_+, \quad \in \partial\Omega_F \tag{7}$$

where $\partial\Omega_F$ is the interface between the fault and the host rock. This formulation allows us to consider the flow along the fault on one side, although the flow across the fault is impeded ($p_+ \neq p_-$). It is valid if fractures are more permeable than the surrounding porous matrix [50,53–55].

2.3. Frictional strength and resistance of faults

We assume that the rock friction follows the Amontons–Coulomb theory. The frictional strength, τ^*, on a static and cohesionless contact interface is given by $\tau^* = \mu|\sigma'_F|$ [56–58], where μ is the friction coefficient. The relation between these Coulomb magnitudes and the shear stress acting on the contact plane, τ, depends on the sliding state. There are three sliding states [52,59]: (1) initially the fault is at rest while the frictional strength is higher than the shear stress acting on the fault, $\tau^* > \tau$, (2) the fault is sliding at quasi-static regime when the frictional strength equals the shear stress acting on the fault, $\tau = \tau^*$, and lastly (3) the fault is sliding

at fully dynamic slip regime when the frictional strength is different than the shear stress acting on the fault, $\tau \neq \tau^*$. In the last case, the excess shear stress acting on the contact surface, $\tau - \tau^*$, induces accelerations.

Under the presence of pore fluids, the frictional strength depends on the effective normal stress, σ'_F, given by:

$$\sigma'_F = T_{n,F} + \alpha_B p^*_F, \tag{8}$$

where p^*_F is the fault pore pressure and $T_{n,F}$ is the total normal stress between the fault surfaces. We calculate frictional strength using the maximum pressure on both sides, $p^*_F = \max(p_+, p_-)$, which implies evaluating the weaker frictional strength. This choice is justified by Jha and Juanes [55], and [60], which argues that it is the most realistic assumption since using the arithmetic average leads to incorrect predictions of fault stability. This criterion is also supported by studies of the internal structure of the fault [41,44], which indicate that the core of the fault is generally less permeable than the damaged zones on both sides. This prevents transverse flow across the fault but allows longitudinal flow [61]. Fault slip occurs along the weakest interface of the fault core, specifically the side with the highest pore pressure. Even if the side with the maximum pore pressure varies along the fault, there will always be an interface available for slip [60].

Since we study the onset of slip driven by fluid injection, faults are initially at rest, i.e., $V = 0$. The characterization of the onset of slip at an initially stationary interface has been a longstanding open problem in solid mechanics [57,62], and in particular as regards the modeling in the context of rate-and-state friction and slip stability [63–67]. Traditional versions of rate-and-state laws present a mathematical singularity at $V = 0$. Here, we compute the friction coefficient, μ, through a simplified version of the regularized rate-and-state model proposed by Yang et al. [68] and based on the traditional formulation of Dieterich [69]; Ruina [49]. The equation reads as follows:

$$\mu(V, \theta) = \mu_0 + a \ln\left(\frac{V + V_0}{V_0}\right) + b \ln\left(\frac{\theta V_0}{D_c}\right). \tag{9}$$

In the above equation, μ_0 is the steady-state friction coefficient at the onset of slip, a is the direct effect friction parameter, b is the evolution friction parameter, D_c is the characteristic slip length over which fault strength evolves [70], and θ is the state variable. Positive values of $(b - a)$ correspond to velocity-weakening friction behavior that favors unstable slip, whereas negative values indicate that stable slip is expected [49,71,72]. Here V_0 is the reference velocity, with $\theta^* = D_c/V_0$ being the initial value of the state variable. Although V_0 is defined as an arbitrary creep velocity in classical rate-and-state laws, in regularized models it serves as a threshold for small slip velocities to avoid the singularity at $V = 0$. A detailed study of the effects of regularization for several values of V_0 can be found in [73].

The evolution of the state variable can be simulated through different models. Here, we adopt the regularized form of the Dieterich–Ruina aging law [68] that captures the observed time-healing mechanism of contact surfaces [49,69,70,74]. The law reads:

$$\frac{d\theta}{dt} = 1 - \frac{(V + V_0)\theta}{D_c}. \tag{10}$$

2.4. Numerical implementation

Our mathematical model is coded using COMSOL Multiphysics [75], a finite-element software. We solve in a monolithically-coupled fashion the field Eqs. (1)–(6) together with the rate-and-state model (9)–(10) [50,51,73] using the finite element method. Frictional contact on the fault is solved using an Augmented Lagrangian formulation [75] in a monolithically-coupled fashion.

The domain is discretized with triangular elements. Interpolation functions are quadratic Lagrangian for displacements and linear for pore pressure on the host rock. Pore pressure inside the fault is simulated with linear elements using linear interpolation functions. Time integration is fully implicit and adaptive and employs a second-order backward differentiation formula [76]. The time step ranges from 1 h before the fault reactivation to a few milliseconds during the rupture.

2.5. Analytical solution: pressure diffusion and critical pressure

Fluid pressure on a porous material can be computed using analytical solutions under several assumptions and simplifications. Analytical solutions to compute the stress response to pore pressure variations in reservoirs are developed for the case of a finite reservoir embedded in an infinite domain crossed by a non-displaced fault [77–82], displaced but permeable faults [83] or displaced and low-permeable fault [84]. The latter solution was extended to the half-space domain to consider the effect of the ground surface [85]. However, quasi-steady uniform changes in pore pressure are assumed in the reservoir *i.e.*, as these solutions are found using inclusion theory. The reservoir is modeled as an inclusion in an infinite domain, which requires the assumption that no pressure change occurs in the surrounding rocks; *i.e.*, there is no hydraulic flow [80].

Analytical solutions are available to compute the stress response to variations in pore pressure in infinite reservoirs with point sources. Barry and Mercer [86] developed an analytical solution for the time-dependent two-dimensional flow and deformation of a square poroelastic material with a point source. The solution does not account for the effect on the flow of an impermeable fault. However, it applies to our problem with faults with the same permeability values as the host rock. If poroelastic effects are neglected, the pore pressure p in a 2D porous elastic material with a constant point source q is given by Theis' analytical solution [87–89]. Pore pressure at a given time t is computed with:

$$p(r, t) = \frac{q\eta_f}{4\pi k} E_1\left(\frac{r^2}{4Dt}\right), \tag{11}$$

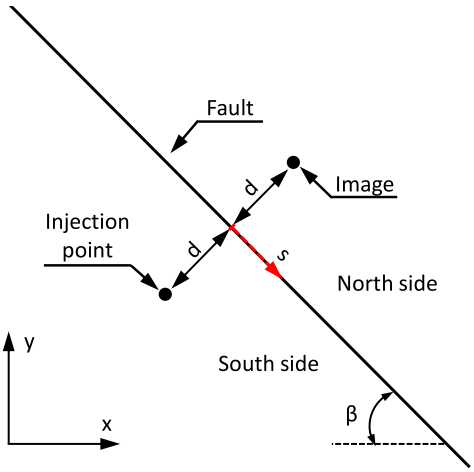

Fig. 1. Scheme of the fault and the injection point. We consider an infinite impermeable fault embedded in a porous elastic host rock, *i.e.*, Biot coefficient is zero. s is the spatial coordinate along the fault, d is the distance from the injection point to the fault, and β is the orientation of the fault. Fluid is injected at a constant flow rate q through an injection point located on the south side of the domain. Pore pressure is computed using Theis' analytical solution, and we include an image on the north side of the domain to consider the impermeable effect of the fault. Pore pressure on the north side is zero since the fault is impermeable and poroelastic effects are neglected. In contrast, pressure on the south side of the domain is computed using Theis' analytical solution with two injection points, the real one on the south side and its image on the north side.

where q is the injection flow rate per unit length in the perpendicular direction of the domain, η_f is the fluid dynamic viscosity, k is the intrinsic permeability, r is the distance to the injection point, t is time, $D = k/S/\eta_f$ is the hydraulic diffusivity, S is the storage coefficient, and E_1 is the exponential integral function, given by:

$$E_1(x) = \int_x^\infty \frac{e^{-\delta}}{\delta} d\delta. \tag{12}$$

Using Eqs. (11) and (12) and neglecting poroelasic effects, we compute the pore pressure distribution on an infinite and impermeable fault embedded in a porous elastic host rock. Fig. 1 includes a scheme of the problem to solve. Fluid is injected into the rock through an injection point on the south side of the domain, as shown in the figure. Since the fault is impermeable and poroelastic effects are neglected, pore pressure on the north side is zero. In contrast, pressure on the south side is computed using Theis' analytical solution (Eq. (11)) with two injection points, the real one on the south and its image on the north. The image source simulates the impermeable impact of the fault on the fluid flow, which cannot flow through the fault to the north side. Pore pressure distribution on the south side of the fault is then given by:

$$p(r,t) = 2\frac{q\eta_f}{4\pi k} E_1\left(\frac{r^2}{4Dt}\right), \tag{13}$$

where r is the distance from the injection well to the considered point of the fault. Eq. (13) is valid only on the fault and not in the host rock.

The critical pressure required to reactivate the fault is determined by the tectonic stresses, given by σ_x and σ_y on the global reference system (x, y) included in Fig. 1. Normal and shear stress on a fault, σ_0 and τ_0, with orientation β are computed with:

$$\sigma_0 = \frac{\sigma_y + \sigma_x}{2} + \frac{\sigma_y - \sigma_x}{2}\cos(2\beta), \tag{14}$$

and

$$\tau_0 = \frac{\sigma_x - \sigma_y}{2}\sin(2\beta). \tag{15}$$

In the absence of poroelastic effects, the critical pressure required to reactivate fault is then:

$$p_{crit} = \sigma_0 - \frac{\tau_0}{\mu_0}, \tag{16}$$

where μ_0 is the friction coefficient.

3. Simulation setup

Our domain is a 10 km side-square, which represents a horizontal 2D section of a three-dimensional homogeneous porous formation intersected by a fault plane oriented at β=30° to the x-axis, with an injection well located on the south side of the fault at a given distance d from the fault – Fig. 2(**a**). We impose a volumetric flux on the boundary of the injection well, a 5 m-radius

circle. For illustration purposes, we overlay a contour plot of the undrained pressure response during rupture propagation in Fig. 2(**a**). Before the earthquake rupture, the pore pressure on the south side of the fault changes mainly due to fluid injection, whereas during rupture it changes mainly due to the poroelastic effects. However, since we simulate an impermeable fault, the pore pressure on the north side only changes due to poroelastic effects during all phases of the earthquake.

The permeability, porosity, Young's modulus, and Poisson's ratio of the rock are $k = 10^{-14}$ m^2, $\phi = 0.1$, $E = 20$ GPa, and $\nu = 0.25$, respectively. The fluid density, dynamic viscosity, and compressibility are $\rho_f = 1000$ kg/m^3, $\eta_f = 0.001$ Pa·s, $\chi_f = 4 \cdot 10^{-10}$ Pa^{-1}, respectively. These hydromechanical parameter values fall within the typical thresholds for sandstone [90]. The Biot coefficient accounts for the poroelastic coupling and is set to one, $\alpha_B = 1$.

The boundary conditions are zero x–displacement on the left boundary and zero y–displacement on the bottom boundary, as shown in Fig. 2(**a**). On the right and top boundaries, we impose tectonic loads according to the regional stress state and the tectonic ratio. In our simulations, the tectonic loads are $\sigma_y = 5$ MPa, and σ_x, which varies depending on the tectonic ratio σ_x/σ_y. We adopt plain-strain conditions.

We impose a constant reference pressure, $p = 0$, on the right boundary and no flow on the other boundaries. On the boundary of the injection well we impose an input flow velocity $v_0 = 20$ mm/h. We simulate the change in friction coefficient with the aging law – Eq. (10) – with rate-and-state parameters $a = 0.005$, $b = 0.02$, $D_c = 200$ μm, $V_0 = 10^{-9}$ m/s, and $\mu_0 = 0.6$. These frictional parameters, typically the most challenging to measure in practice, are reasonable values widely cited in the literature [52,73].

We discretize the domain with an irregular triangular mesh, as shown in Fig. 2(b). The elements are 2-m long near the fault to capture the physics of the discontinuity, and the size increases up to 200 m on the boundaries. This mesh size on the fault is lower than the Dieterich nucleation length scale, given by Ampuero and Rubin [91]:

$$L_b = \frac{G}{1-\nu}\frac{D_c}{b\sigma'_F}, \tag{17}$$

which according to the initial effective normal stress on the fault, σ'_F, given by Eq. (13) and the simulation parameters, L_b is approximately 20 m. The elements around the injection well are 1 m in length. We adopt quadratic Lagrangian interpolation functions for displacements and linear interpolation functions for pore pressure.

4. Results and discussion

We perform simulations with our 2D numerical poroelastic model for $d = 50$, 100, 150 and 200 m and tectonic ratios $\sigma_x/\sigma_y = 2.0$, 2.5 and 2.9. We also run an extra simulation for $\sigma_x/\sigma_y = 2.0$ and $d = 400$ m as an almost unilateral case.

4.1. The role of poroelasticity on rupture directivity

In our simulations, we identify two poroelastic mechanisms governing the symmetry of the rupture. The first one occurs before the onset of slip and depends on the shape of the pore pressure bell distribution on the fault. The second is related to the undrained coseismic response during the rupture, *i.e.* during the fault slip.

4.1.1. Pore pressure distribution at the onset of slip

We illustrate the effect of both poroelasticity and distance between the fault and the injection well on the stress profiles along the fault at the onset of slip in Fig. 3. Initially, the fault is at rest. Frictional strength and shear stress acting on the fault are given by the tectonic stress, as shown in Fig. 3 (**a**). Before the reactivation and during the injection, the friction coefficient remains constant, so the change in frictional strength is only produced by the increase in pore pressure and evolves towards the bell-curve shape shown in Fig. 3 (**b**) — red lines. Shear stress on the fault adopts a double-soliton shape, $\cong xe^{-x^2}$, profile due to poroelastic effects that make the rock around the injection well expand — blue lines.

The onset of slip takes place when the shear stress on the fault equals frictional strength, green points in Fig. 3 (**c**). The point where the fault starts to slip moves away from the midpoint of the fault as the pore pressure profile on the fault at the onset of the slip is wider. Since the shape of the pore pressure profile at the reactivation time is controlled by the distance between the injection well and the fault, changing this value from $d = 50$ m, solid lines in panel (**c**), to $d = 400$ m, dashed lines in panel (**c**), makes the rupture initially more asymmetric.

In conclusion, poroelastic effects and the distance between the injection well and the fault promote an asymmetric onset of slip. The grade of asymmetry grows as the injection well is further from the fault, or the injected volume to reactivate the fault increases.

4.1.2. Undrained response during the rupture

We analyze the propagation of the rupture fronts during coseismic earthquakes to detect asymmetry patterns. The fault's slip deforms the host rock, causing positive or negative strains that decrease or increase pore pressure, respectively. Since ruptures in our simulations last approximately 1 s, while diffusion times are on the order of days ($t_d = d^2 S\eta_f/k \sim 10^5$ s), the deformation of the host rock is so fast that fluid cannot flow and, consequently, the divergence in Eq. (1) is negligible, *i.e.*:

$$\nabla \cdot \left(-\rho_f \frac{k}{\eta_f}\nabla p\right) \approx 0, \tag{18}$$

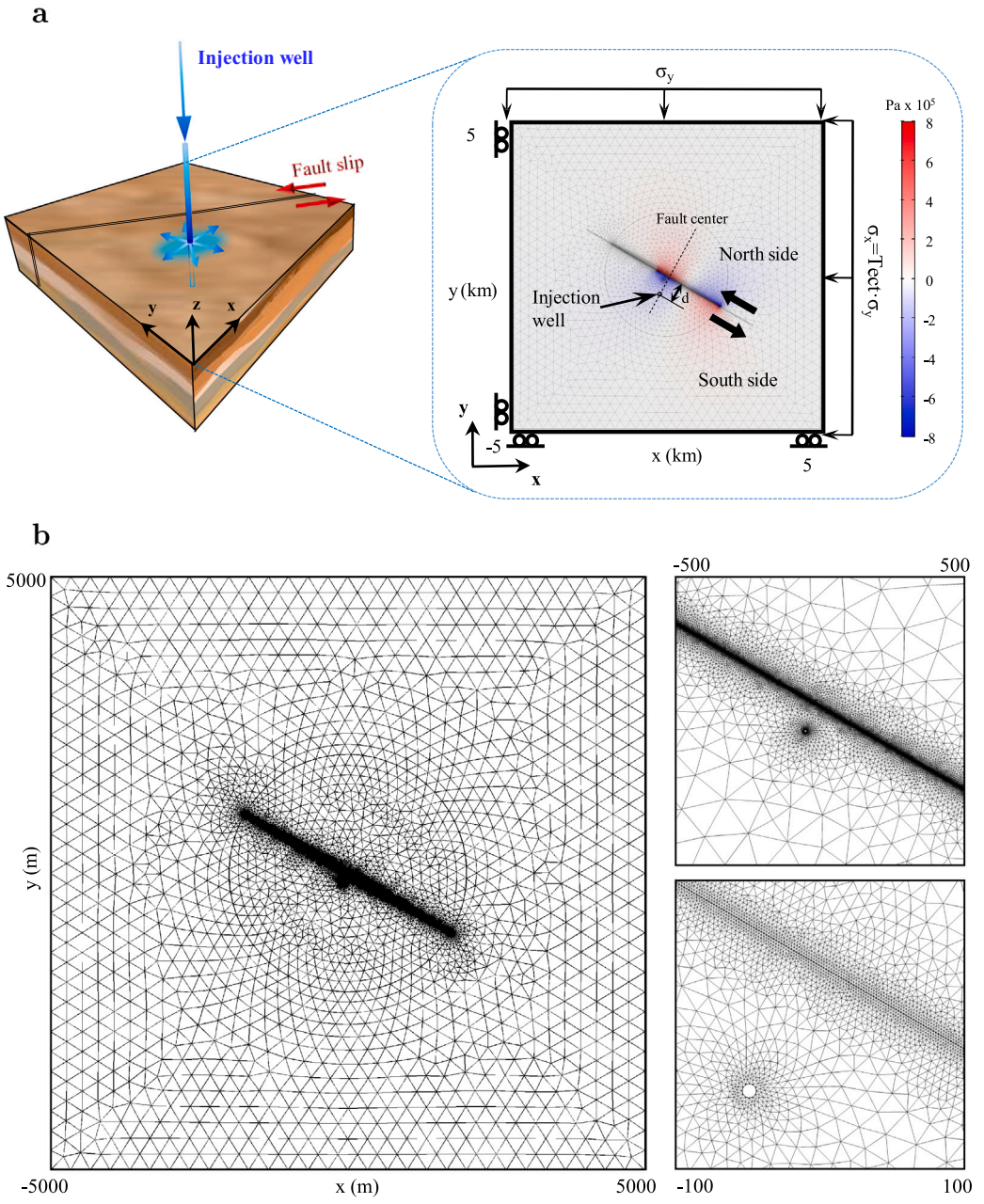

Fig. 2. Numerical model setup for hydromechanical simulations. (**a**) Our conceptual model is a strike-slip frictional fault of length 4000 m. We simulate a horizontal 2D squared poroelastic domain of 10 km side. Fluid is injected through an injection well of a 5 m radius circle located at a d-distance from the fault. We denote the south side of the fault as the injection side. Tectonic stresses are applied on the boundaries, $\sigma_y = 5$ MPa, and several tectonic ratios σ_x/σ_y. For illustration purposes, we overlay the scheme of the 2D domain with a plot of the pore-pressure field at a given time during the rupture propagation. The change in pressure on the north side of the fault is the undrained response due to the sudden deformation of the host rock during rupture and it emerges as a result of the poroelastic effects. (**b**) We discretize the domain with an irregular triangular mesh. The elements are 2 m in length near the fault and the size increases up to 200 m on the boundaries. The elements around the injection well are 1 m in length.

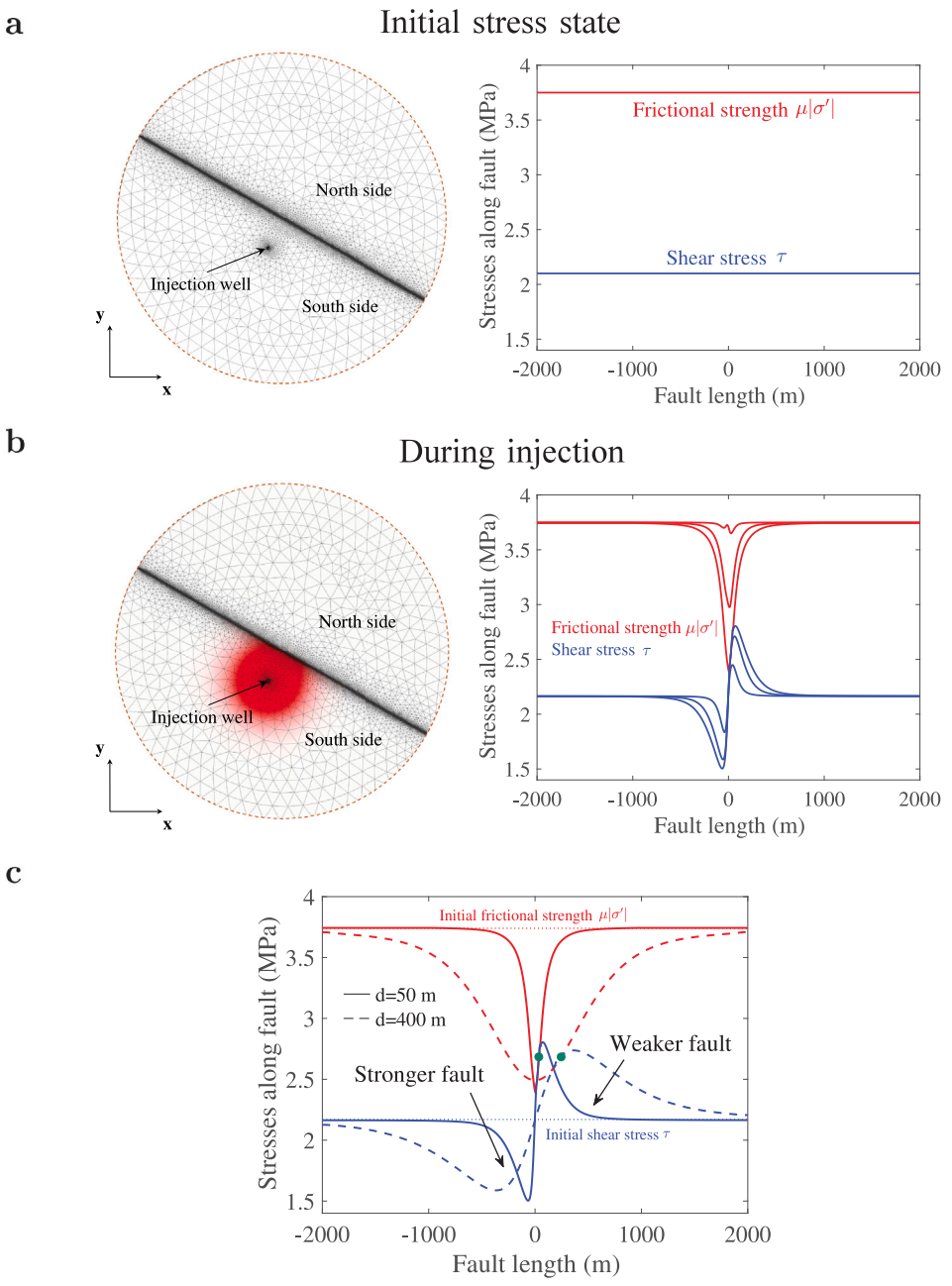

Fig. 3. Ilustration of the effect of the pore pressure distribution at the onset of the slip on the rupture directivity. In (**a**) we plot the frictional strength $\mu\sigma'$ and shear stress τ at the onset of injection for $d = 50$ m and tectonic ratio $\sigma_x/\sigma_y = 2.0$. In (**b**) we plot the frictional strength $\mu\sigma'$ and shear stress τ during the injection and before the reactivation. The circles on the left represent insets of the 2D model in the fault zone, showing the mesh and the pore pressure field to illustrate the diffusion during the injection. In (**c**) we plot both frictional strength and shear stress for two cases distances between the fault and the injection well $d = 50$ m (solid lines) and $d = 400$ m (dashed lines). The tectonic ratio is $\sigma_x/\sigma_y = 2.0$ in both cases. The green points are the segment where the slip starts, *i.e.* the hypocenter of the earthquake.

and Eq. (1) turns into:

$$\rho_f S \frac{\partial p}{\partial t} + \rho_f \alpha_B \frac{\partial \epsilon_v}{\partial t} = 0, \tag{19}$$

that simulates the undrained response produced by the poroelastic effect.

This explains the onset of two undrained pressure fronts that propagate along the fault in opposite directions. Since we simulate impermeable faults, fluid does not cross the fault and pressure on both sides is different. During the rupture, the undrained response

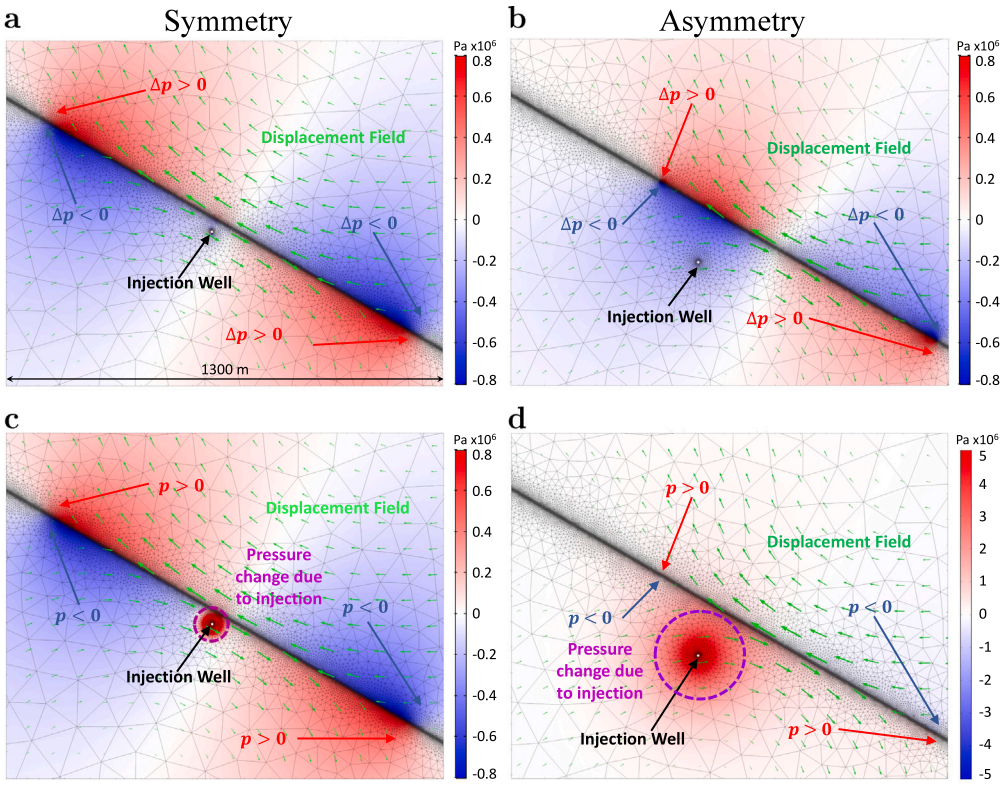

Fig. 4. Illustration of the undrained effect during the rupture propagation for $d = 50$ m and $\sigma_x/\sigma_y = 2.9$ in panels (**a**) and (**c**), and for $d = 200$ m and $\sigma_x/\sigma_y = 2.0$ in panels (**b**) and (**d**). Panels (**a**) and (**b**) depict the increase in pore pressure during the rupture, taken as reference the pore pressure at the onset of slip, and panels (**c**) and (**d**) plot the total pore pressure at the same time step as panels (**a**) and (**b**), respectively. Red colors represent increases in pore pressure and blue colors decrease. Green vectors represent the displacement field. Case in panels (**a**) and (**c**) is the most symmetric rupture in our numerical simulations, whereas case in panels (**b**) and (**d**) is the most unilateral rupture. For the most symmetric case, the magnitude of the pressure front is approximately equal to the injection pressure. Still, for the unilateral case, the magnitude of the pressure front is small compared with the injection pressure.

makes pore pressure change in opposite directions, *i.e.* pressure increases in some areas and decreases in others, as shown in Fig. 4 (**a**) and (**b**).

We illustrate the underlying phenomena in Fig. 4, where we plot the results of pressure distribution for the simulation with the most symmetric rupture $-\sigma_x/\sigma_y = 2.9$ and $d = 50$ m– in panels (**a**) and (**c**) and for an asymmetric rupture $-\sigma_x/\sigma_y = 2.0$ and $d = 200$ m– in panels (**b**) and (**d**). The displacement field is plotted with green vectors. Panels (**a**) and (**b**) depict the pore pressure profile at a given time step during the rupture minus the pressure at the onset of slip. The undrained response mainly produces the change in the pressure during the rupture. We plot the total pore pressure at the same time step in panels (**c**) and (**d**) of Fig. 4.

The poroelastic effect explains the onset of two undrained pressure fronts that propagate along the fault in opposite directions. Since we simulate impermeable faults, fluid does not cross the fault and pressure on both sides is different. During the rupture, the undrained response makes pore pressure change in opposite directions, *i.e.* pressure increases in some areas and decreases in others, as shown in panel (**a**) and (**b**) of Fig. 4.

Fig. 4 also reveals a trend towards symmetry rupture fronts as the tectonic ratio increases. Since $\sigma_y = 5$ MPa in all our simulations, an increase in the tectonic ratio implies that the fault is initially closer to the reactivation and most of the change in pore pressure is generated by the poroelastic effects associated with the undrained response during the rupture. Moreover, rupture propagation tends to the symmetry, since the initial asymmetric shear stress at the onset of slip affects a shorter fault segment due to the lower injection time to trigger the slip on the fault. Therefore, the undrained coseismic response is relevant to controlling the rupture directivity.

4.1.3. Understanding the coupling of poroelastic effects

We observed that the rupture directivity is determined by the distribution of pore pressure at the onset of the slip and the undrained response during the rupture. We illustrate the coupling between the poroelastic effect and the pressure distribution at the onset of slip in Fig. 5. In panel (**a**) we plot the total pressure on both sides of the fault; p_+ on the south side in blue lines, p_- on the north side in green lines, and the maximum of them $p_{max} = \max(p_+, p_-)$ in red lines; for an almost unilateral rupture propagation with $\sigma_x/\sigma_y = 2.0$ and $d = 400$ m. In panel (**b**) we plot p_-, p_+, and p_{max} for a symmetric rupture with $\sigma_x/\sigma_y = 2.9$ and $d = 50$ m.

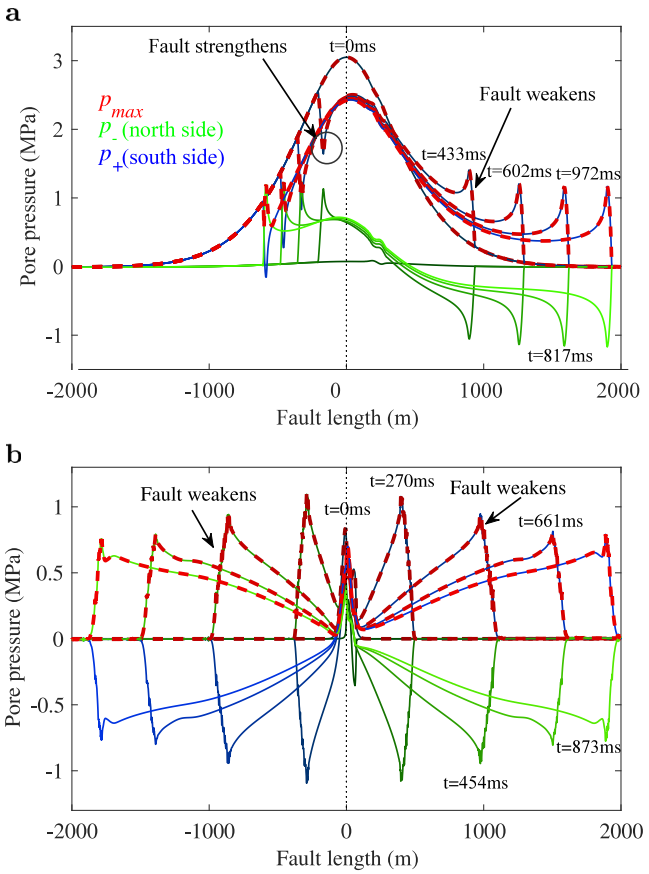

Fig. 5. Illustration of the coupling poroelastic effects. Here we plot the total pressure profiles at several times steps of two ruptures: in panel (**a**) we plot the pressure profiles for a case with $d = 400$ m and $\sigma_x/\sigma_y = 2.0$, and in panel (**b**) for $d = 50$ m $\sigma_x/\sigma_y = 2.9$. Blue lines depict the pore pressure at the south side of the fault, p_+, green lines the pressure at the north side, p_-, and red lines the maximum of both of them $p_{max} = max(p_+, p_-)$. Time is measured in milliseconds and $t = 0$ is the onset of slip.

At the beginning of the simulations, the fault is at rest, $V = 0$, and the fluid injection starts. The fluid flows around the injection well increasing the pore pressure and the pressure profile on the fault takes the bell-curve shape depicted in Fig. 5 until the fault reactivation (time $t = 0$ in Fig. 5). The poroelastic effect makes the hypocenters move to the right side of the fault, as explained in Section 4.1, and consequently, the rupture begins with an initial asymmetry. Then the slip propagates along the fault with a pattern analogous to two crack tips spreading from the hypocenter, creating two pore pressure fronts moving along the fault in opposite directions.

During the first stages of the rupture, the pore pressure adopted to calculate the effective normal stress on the right side of the fault is p_+ since $p_+ > p_-$, as shown in panels (**a**) and (**b**) for both cases. The undrained response increases pressure, and the right tip overpressure ($\Delta p > 0$) weakens the fault. On the contrary, the pore pressure used to calculate the effective normal stress on the left side of the fault is p_-, and the undrained response makes the pressure decrease and the left tip overpressure ($\Delta p < 0$) strengthens the fault. The strengthening phenomenon is more pronounced as the pressure bell at the onset of slip is wider, as shown in panel (**a**), and may almost disappear for extremely narrow pressure bells at the onset of slip, as happened in the case plotted in panel (**b**). This pattern of weakening and strengthening determines the propagation of the rupture front: fault strengthening at the left front arrests its propagation, but the right tip moves faster due to the fault weakening.

Once the rupture advances and the left front surpasses the bell-curve zone of the pressure profile at the reactivation, the strengthening phenomenon disappears. Then, the pressure value to calculate the effective normal stress is the pressure on the north side of the fault as $p_- > p_+$. Then, in the advanced stages of the rupture, both fronts propagate with the same velocity. Therefore, the asymmetry in rupture propagation depends on the size of the pressure bell at the onset of the slip.

In contrast to the weakening and strengthening patterns that lead to asymmetric ruptures, if the pressure distribution at reactivation is extremely narrow, as shown in panel (**b**), the strengthening pattern disappears almost immediately. Then, both fronts propagate at the same speed and the rupture is almost symmetric, as shown for the case in panel (**b**).

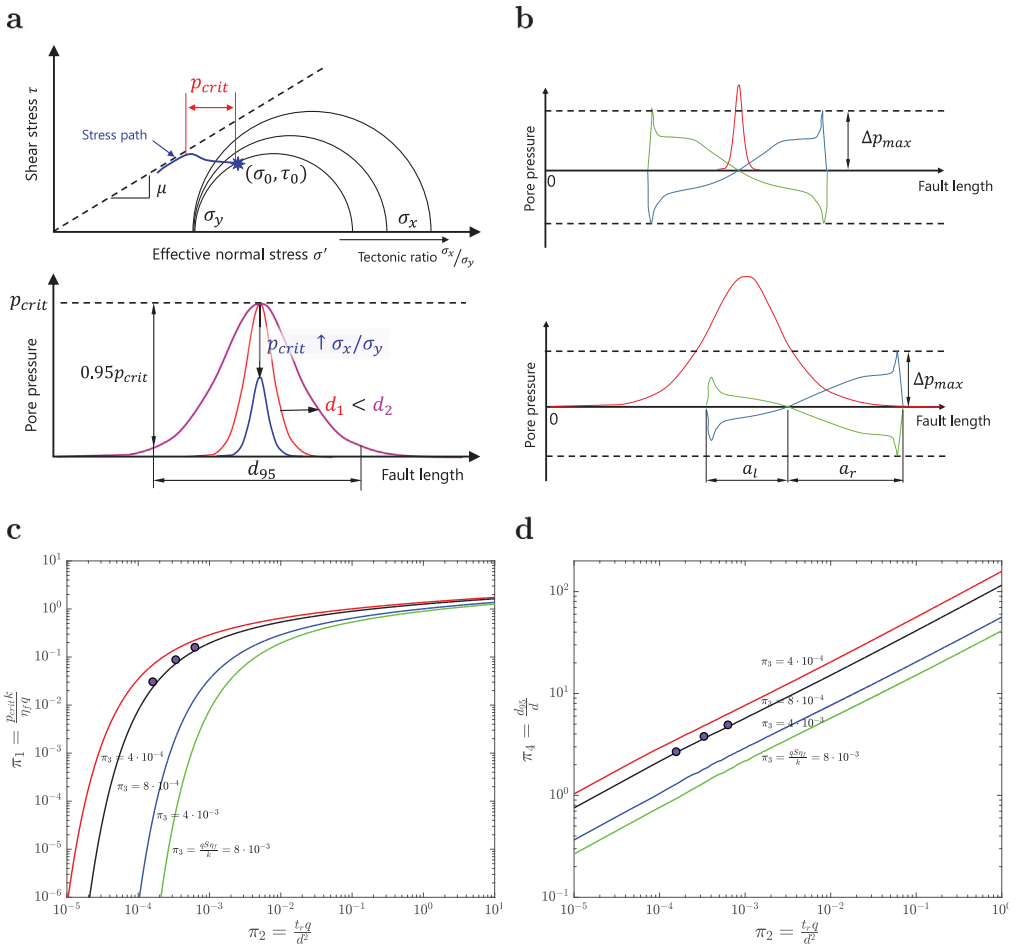

Fig. 6. Influence of the tectonic ratio and the undrained response in the rupture directivity. Panel (**a**) depicts the influence of the tectonic ratio on fault reactivation: at higher tectonic ratios, for a fixed vertical stress σ_y, the Mohr circle radius increases, the circle approaches the failure envelope and then the critical pressure that is needed to reach the reactivation decreases. Panel (**b**) illustrates the pressure profile on the fault at the onset of slip with the red lines, the undrained pressure response on the north side of the fault with the blue lines, and on the south side with the green lines. In both schemes, there are two opposite rupture fronts due to undrained coseismic pressure response with the same peak magnitude (blue and green lines). The width and peak value of the pressure distribution at reactivation (red lines) determine its predominance over the undrained pressure front, promoting symmetric (thinner and smaller distributions) or asymmetric (wider and higher distribution) ruptures. Panel (**c**) plots the relationship between the dimensionless parameters π_1 and π_2 for several values of π_3. Panel (**d**) depicts the dimensionless parameters π_4, which encompasses the dimensionless width of the pressure distribution, against the dimensionless parameter π_2 for several hydraulic properties given by π_3. In (**c**) and (**d**) the violet points indicate the values of the dimensionless parameters for numerical simulations.

4.2. Dimensionless analysis of fault-injection system reactivation

We quantify the influence of hydromechanical parameters on the fault reactivation. We perform a parametric sweep to examine the effect of the tectonic ratio, injection flow rate, host rock permeability, and distance between the injection well and the fault on fault reactivation. The impact of these parameters is illustrated in Fig. 6. In panel (**a**) we plot the Mohr–Coulomb diagram for several tectonic ratios and a given failure envelope with μ_0 slope.

If poroelastic effects are neglected, the critical pressure required to reactivate the fault is determined by the tectonic stress, σ_x, and σ_y, and the fault orientation, β, that define the initial normal and shear stress on the fault plane (σ_0, τ_0). For constant σ_y, the radius of the Mohr–Coulomb circle increases with the tectonic ratio and approaches the failure envelope. Consequently, the tectonic ratio controls the critical pressure necessary to reactivate the fault, given by $p_{crit} = \sigma_0 - \tau_0/\mu_0$, and it is independent of the hydraulic properties of the host rock.

The distance between the injection well and the fault controls the width of the pressure distribution along the fault, panel (**a**). For given values of the tectonic ratio and the critical pressure, the width of the pressure bell increases with the distance between the injection well and the fault. We quantify the width of the pressure bell with the distance d_{95}, defined as the width of the pressure bell that exceeds 5% of the critical pressure to reactivate the fault.

The combination of both factors, tectonic ratio and injection distance, control the size of the pressure bell that reactivates the fault, and then the rupture directivity. Higher tectonic ratios and injection points closer to the fault reduce the width of the pressure

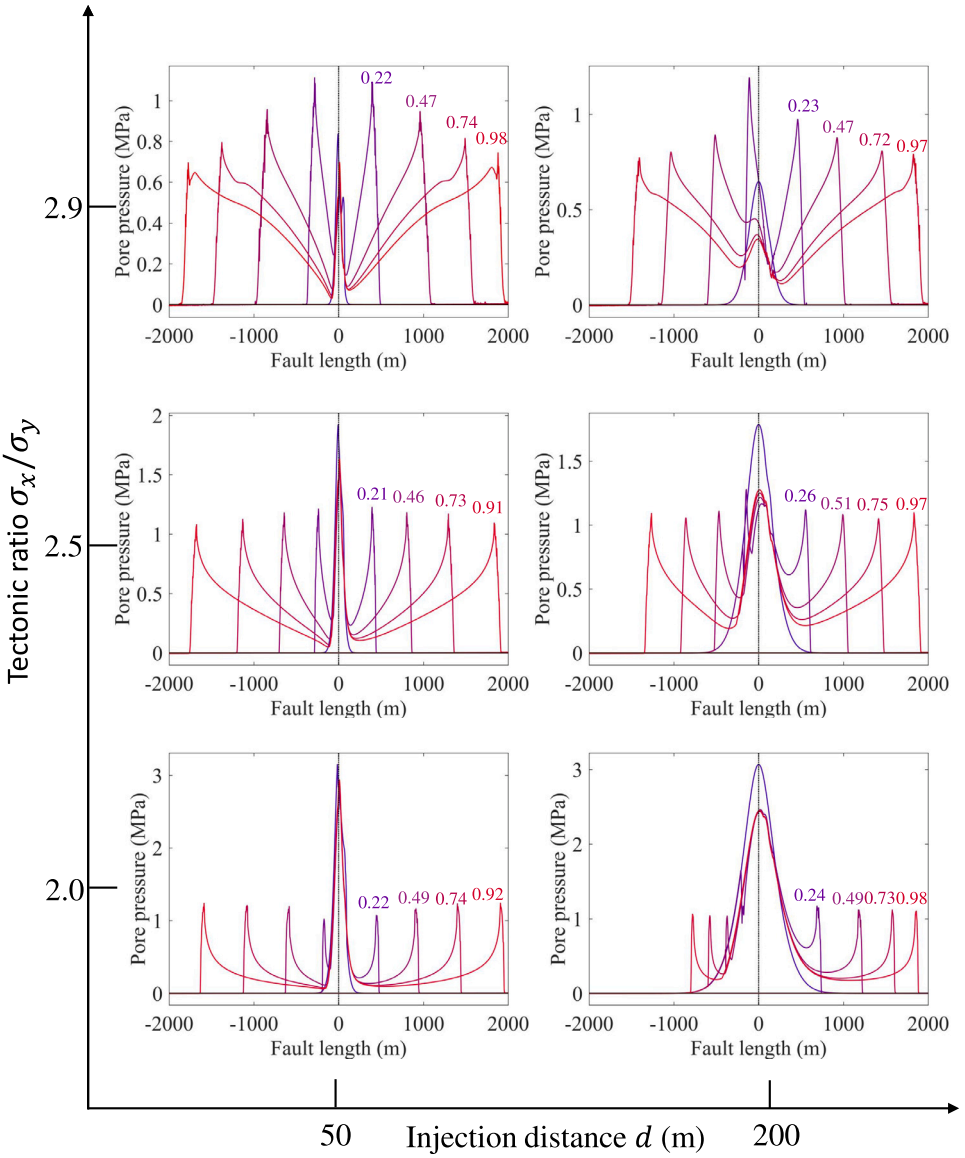

Fig. 7. Pore pressure distribution along the fault at some instants during the seismic rupture, considering the maximum value between both sides of the fault. Summary of the results for different combinations of tectonic ratio ($\frac{\sigma_x}{\sigma_y}$ = 2.0, 2.5 and 2.9) and distance to the injection well (d = 50 m and 200 m). In all cases, the magnitudes of the undrained pressure fronts are similar, around 1 MPa, but the peak pressure value at the beginning of the rupture is higher for lower tectonic ratios, as the fault is initially further from the rupture. The numbers above each undrained pressure peak indicate the relative time elapsed since the beginning of the rupture.

bell to reactivate the fault and favor symmetric ruptures. The undrained pressure fronts prevail over reactivation pressure, panel (**b**). Conversely, lower tectonic ratios increase the critical pressure, leading to wider pressure bells and reducing undrained pressure fronts. Asymmetric ruptures are then favored.

For a given p_{crit}, Eqs. (14)–(16), and using Theis' analytical solution, Eq. (13), we calculate the width of the pressure bell, d_{95}, at the onset of the reactivation, and the reactivation time, t_r, defined as the time required to reach p_{crit} at some point on the fault. Theis' analytical solution disregards poroelastic effects, yet it offers reasonable approximations of p_{crit}, d_{95}, and t_r before the onset of slip, with minimal computational cost.

Table 1 lists some values of the critical pressure and the reactivation time for several tectonic ratios σ_x/σ_y and distances d. We observe that the ratio d/d_{95} is independent of d and only varies with the tectonic ratio. Consequently, the problem may be analyzed in terms of the fault failure based on the initial stress conditions.

The dimensional analysis using the Buckingham π theorem [92], renders three dimensionless parameters: (1) $\pi_1 = p_{crit}k/(\eta_f q)$ encompasses the pressure on the fault and the pressure diffusion on the host-rock, (2) $\pi_2 = t_r q/d^2$ includes the time t_r to reach the

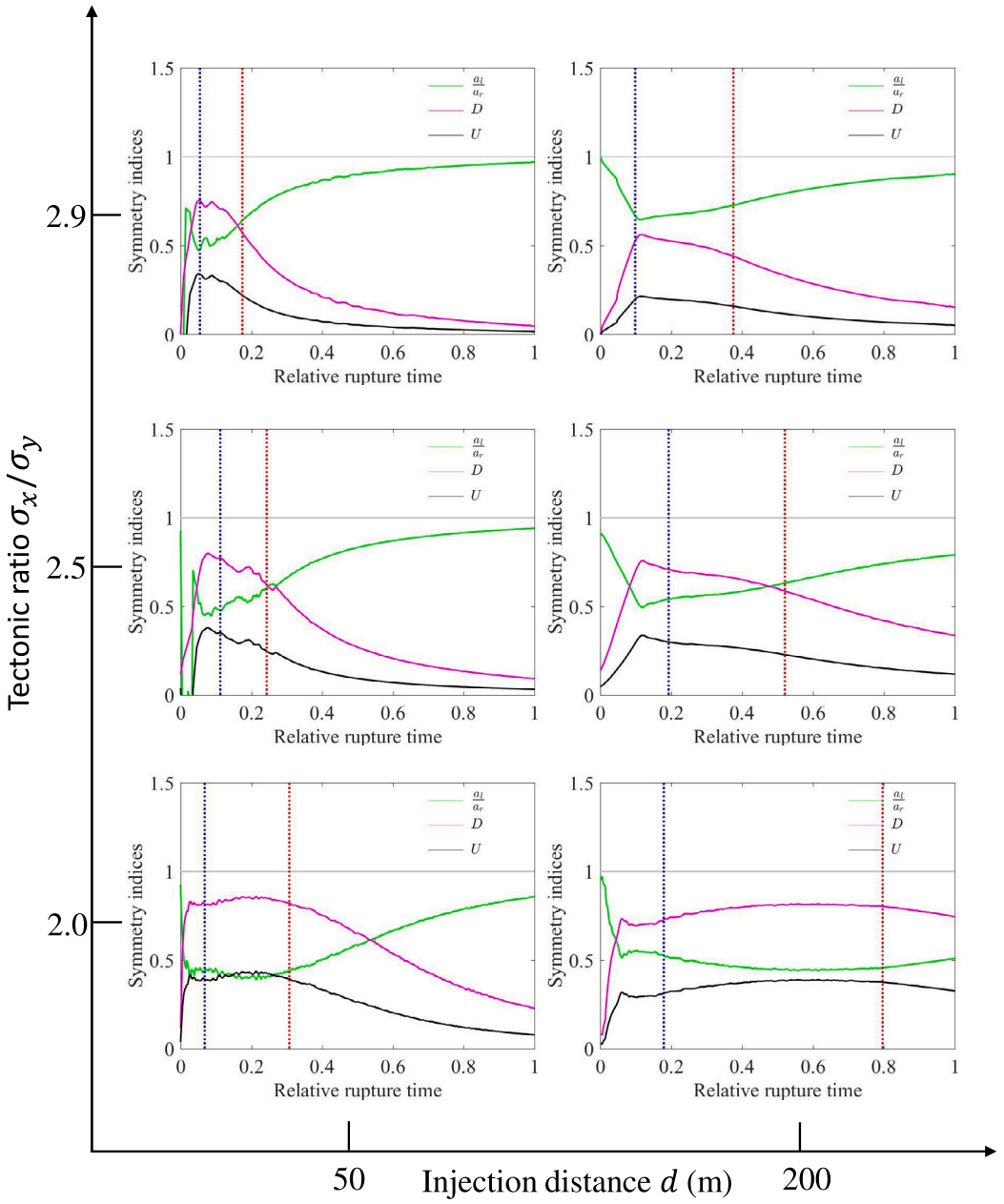

Fig. 8. Evolution of symmetry measures during the rupture propagation. We show the proportion unilateral rupture U (black lines) and directivity ratio D (magenta lines). We also plot the ratio of the advance distances of the rupture tips, $\frac{a_l}{a_r}$. Results are displayed for the same tectonic ratios ($\frac{\sigma_x}{\sigma_y} = 2.0$, 2.5 and 2.9) and distances to the injection well ($d = 50$ m and 200 m) used in Fig. 7. Blue and red vertical dotted lines represent the instants when the right and left rupture fronts, respectively, surpass the reactivation pressure bell (d_{95} area).

pressure p_{crit} at some point of the fault and injection distance d, and (3) $\pi_3 = qS\eta_f/k$ synthesizes the hydraulic properties of the host rock. The fourth dimensionless parameter is $\pi_4 = d_{95}/d$ which is the ratio between the width of the pressure bell, d_{95}, and the distance d of the injection well to the fault.

The relationship between the dimensionless parameters π_1 and π_2 for several values of π_3 is plotted in panel (**c**). For a given critical reactivation pressure p_{crit}, injection rate q, and hydraulic properties included in π_3, the time to reactivation is provided by the curves.

The analysis of panel (**c**) yields two conclusions. (1) For given hydraulic properties, the time to reactivation increases with the increase in the critical pressure and decreases with the increase in the injection flow rate. (2) For a given injection flow rate and

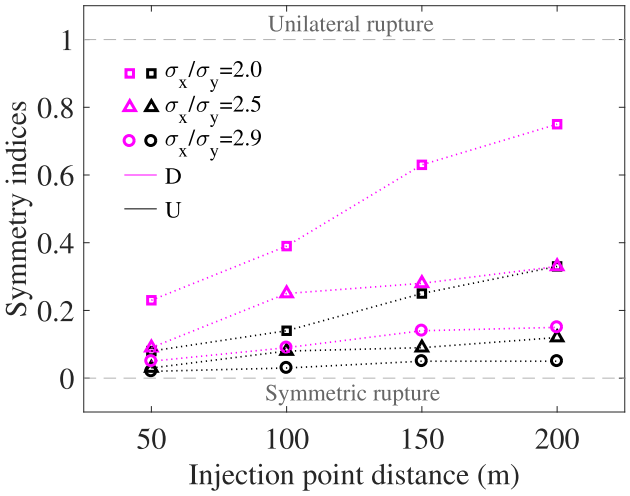

Fig. 9. Summary of proportion unilateral rupture U (black symbols) and directivity ratio D (magenta symbols) at the end of the rupture, for tectonic ratios $\frac{\sigma_x}{\sigma_y}$ = 2.0 (squares), 2.5 (triangles), and 2.9 (circles); and well-distances to the fault d = 50, 100, 150, and 200 m. Horizontal gray dashed lines represent the delimitation of the parametric area studied in the numerical simulations. Values around 1 represent completely unilateral ruptures, while values close to 0 indicate symmetrical ruptures.

Table 1
Dimensionless parameters computed with Theis' analytical solution for the cases simulated with our numerical model.

σ_x/σ_y	d [m]	p_{crit} [MPa]	d_{95} [m]	t_r [d]	π_1	π_2	π_3	π_4
2.0	50	2.64	210	0.10	0.151	0.0006	0.0007	4.20
2.5	50	1.46	162	0.05	0.084	0.0003	0.0007	3.26
2.9	50	0.52	120	0.03	0.030	0.0002	0.0007	2.40
2.0	100	2.64	420	0.41	0.151	0.0006	0.0007	4.20
2.5	100	1.46	326	0.22	0.084	0.0003	0.0007	3.26
2.9	100	0.52	242	0.11	0.030	0.0002	0.0007	2.40
2.0	150	2.64	630	0.92	0.151	0.0006	0.0007	4.20
2.5	150	1.46	490	0.49	0.084	0.0003	0.0007	3.26
2.9	150	0.52	364	0.24	0.030	0.0002	0.0007	2.40
2.0	200	2.64	842	1.64	0.151	0.0006	0.0007	4.20
2.5	200	1.46	654	0.88	0.084	0.0003	0.0007	3.26
2.9	200	0.52	486	0.42	0.030	0.0002	0.0007	2.40

critical pressure, the time to reactivation increases as the permeability of the host rock does, or as the viscosity or the storage coefficient decreases.

The effect of the dimensionless parameters π_2 on the shape of the pressure bell included in π_4 is depicted in panel (**d**) for several hydraulic properties given by π_3. The analysis of the curves draws up two conclusions. (1) For given hydraulic properties, the width of the pressure distribution increases as the injection flow rate or the time to reactivation does. (2) For a given injection flow rate and time to reactivation – or given critical pressure –, the width of the pressure distribution increases as the permeability does or as the viscosity or the storage coefficient decreases.

4.3. Insights into rupture directivity: The role of fault features

4.3.1. Influence of model parameters on rupture directivity

We include a summary of the results provided by our numerical simulations in Figs. 7 and 8 for some combinations of tectonic ratios and injection well distances. Fig. 7 shows the total pore pressure distribution on the fault at some time steps during the rupture. The rupture tends to be symmetrical as the tectonic ratio increases or the distance d decreases. Conversely, the rupture turns almost unilateral for the lowest tectonic ratio and the largest injection well distance.

In all cases, the magnitude of the undrained pressure response during the rupture is similar and approximately equal to 1 MPa. However, the critical pressure at the onset of slip, p_{crit}, increases as the tectonic ratio decreases, since the fault is more stable for lower tectonic ratios. Therefore, the relative effect of the undrained response over the critical pressure decreases as the tectonic ratio rises.

We quantify the degree of relative symmetry of the rupture propagation with two parameters, previously adopted by Dempsey and Suckale [28], or [33], among other authors. The parameters are the proportion unilateral rupture, U, and the directivity ratio,

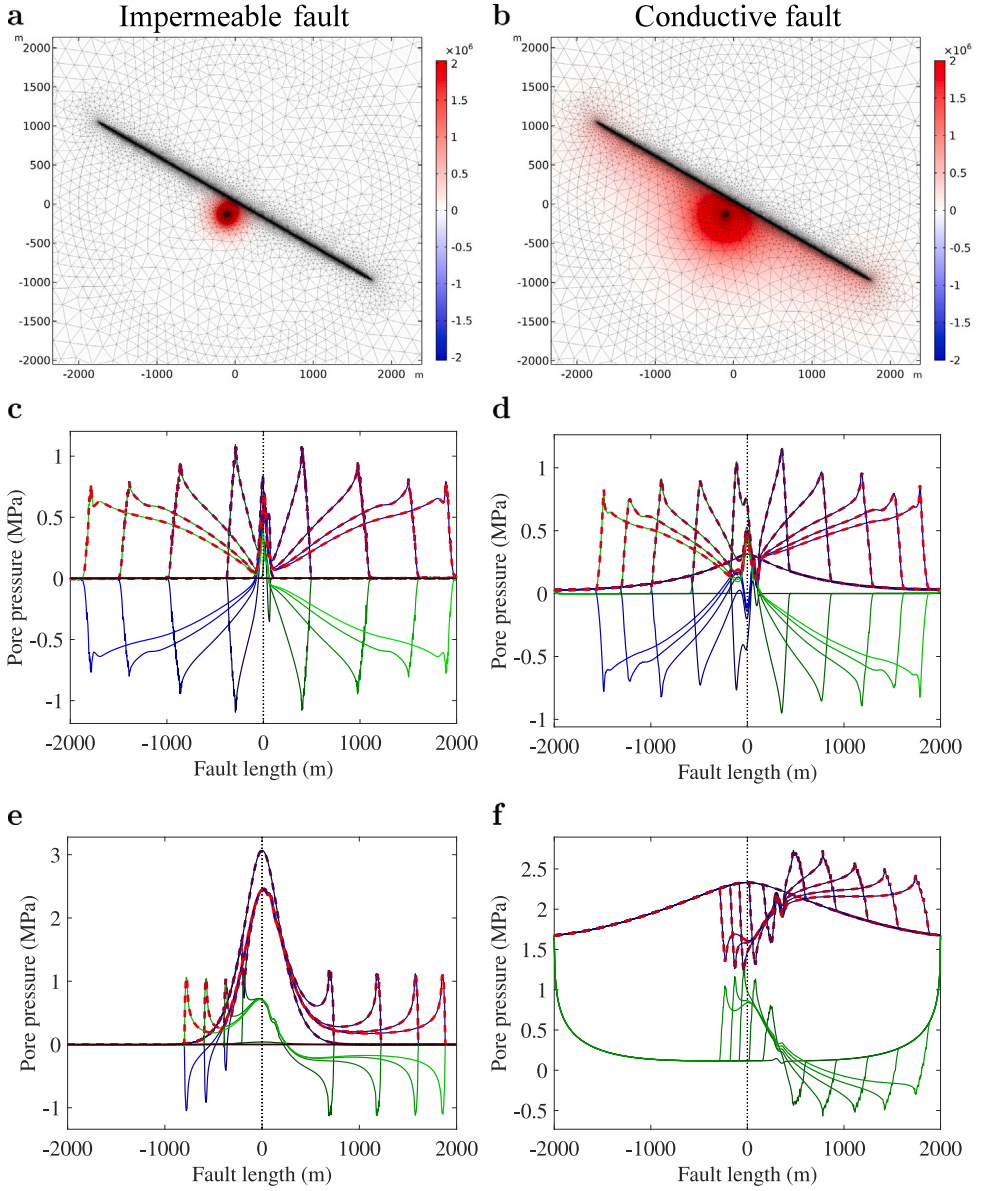

Fig. 10. Here we illustrate the effect of the longitudinal fault permeability on the symmetry of the rupture. Results for the cases with an impermeable fault are included in the left column, and for a longitudinal permeable fault in the right column. In panel (**a**) we plot the contour pressure at the onset of slip for an impermeable fault, and in panel (**b**) for a longitudinal permeable fault. Panels (**c**) to (**f**) depicts the pressure profile at several time steps during the rupture: blue lines depict the pore pressure at the south side of the fault, p_+, green lines the pressure at the north side, p_-, and red lines the maximum of both of them $p_{max} = max(p_+, p_-)$. Pressure profiles computed with $\frac{\sigma_x}{\sigma_y} = 2.9$ and $d = 50$ m, in an impermeable fault are plotted in panel (**c**), and results in a longitudinal permeable fault in panel (**d**). Pressure profiles calculated with $\frac{\sigma_x}{\sigma_y} = 2.0$ and $d = 200$ m in an impermeable fault are plotted in panel (**e**), and results in a longitudinal permeable fault in panel (**f**).

D. They depend on the ratio α between the advance distance of the left and right rupture fronts, a_l and a_r respectively, and the total propagation length, $a_l + a_r$, as shown in Fig. 6 (**b**). The ratio reads:

$$\alpha = \frac{a_l}{a_r + a_l}. \tag{20}$$

The proportion unilateral rupture, U is defined as:

$$U = 1 - 2\alpha, \tag{21}$$

and the directivity ratio, D, is:

$$D = \frac{1 - 6\alpha^2 + 4\alpha^3}{\sqrt{1 - 12\alpha^2 + 24\alpha^3 - 12\alpha^4}}. \tag{22}$$

Both, U and D, theoretically range between -1 and 1. However, we only use the range between 0 and 1 since the sign criterion based on the injection well's location is irrelevant to our study given the symmetry of our problems. In our case, values close to 0 indicate a perfectly bilateral rupture, while values around 1 correspond to totally unilateral ruptures. Due to the configuration of our models, the last case cannot occur but we can achieve relatively high asymmetry values.

We plot the symmetry indices D and U at several time steps during the rupture in Fig. 8. The asymmetry of the rupture is given by the strengthening effect of the left rupture front, while it is within the reactivation pressure bell. After some oscillations during the first instants of the rupture, in all cases, the indices tend quickly to 0 – bilateral symmetrical rupture – when the left rupture front exceeds the reactivation pressure distribution, represented in the plots by the red vertical lines. Symmetrical ruptures have final values around 0, while ruptures with marked asymmetry maintain relatively high values of D and U.

Appendix A includes the pore pressure profiles, the proportion unilateral rupture U, and the directivity ratio D, for the distances $d = 100$ and $d = 150$ m . The transition from symmetrical ruptures to asymmetric ones is shown in more detail. Here we summarize the information about the symmetry indices in Fig. 9, which depicts D and U at the end of the rupture, for all tectonic ratios and well-distances.

4.3.2. Influence of fault conductivity on rupture directivity

Fault conductivity along the contact influences the rupture directivity. We study the effect of longitudinal fault conductivity by performing two new simulations with high longitudinal fault permeability, but impermeable in the transversal direction. The hydraulic properties of the fault material are: permeability $k_F = 10^{-9}$ m^2, thickness $d_F = 0.1$ m, porosity $\phi_F = 0.1$, fluid density $\rho_f = 1000$ kg/m^3, dynamic viscosity $\eta_f = 0.001$ Pa·s, storage coefficient $S_F = 4 \cdot 10^{-11}$ Pa^{-1} and fluid compressibility $\chi_f = 4 \cdot 10^{-10}$ Pa^{-1}. Faults are impermeable in the transversal direction which means that the flow along the fault is only implemented on the south side and pressure changes on the north side are due to poroelastic effects and not due to mass transfer. The first simulation is a symmetric rupture with $\sigma_x/\sigma_y = 2.9$ and $d = 50$ m, and the second case is an asymmetric rupture with $\sigma_x/\sigma_y = 2.0$ and $d = 200$ m. Pore pressure plots are included in Fig. 10.

We plot two pressure contour plots at the onset of the slip in panels (**a**) and (**b**). The results in panel (**a**) are computed with an impermeable fault in both directions, whereas in panel (**b**) with a longitudinal permeable fault. The increase in the longitudinal permeability delays the onset of the slip, as the fluid flows along the fault, and increases the pore pressure in a wider area than the completely impermeable fault.

Pressure profiles computed with $\frac{\sigma_x}{\sigma_y} = 2.9$ and $d = 50$ m in an impermeable fault are plotted in panel (**c**), and results in a longitudinal permeable fault in panel (**d**). The selected tectonic ratio and distance between the injection well and the fault lead to the most symmetric rupture propagation fronts. However, the longitudinal fault permeability induces some asymmetry in the rupture propagation. The left rupture front propagates further in the impermeable fault – panel (**c**) – than in the longitudinal permeable fault — panel (**d**).

The enhancement of asymmetry in the longitudinal permeable fault is explained by the width of the pressure bell on the fault at the onset of the slip. Bells are wider in longitudinal permeable faults than in impermeable faults. In Section 4.1.3 we report that the strengthening phenomenon during the rupture propagation during the first steps is more pronounced as the pressure bell at the onset of slip is wider, and almost disappears for extremely narrow pressure bells. We also report that the strengthening phenomenon induces asymmetrical rupture fronts. Consequently, the strengthening phenomenon is stronger in longitudinal permeable faults due to the wider pressure bell at the onset of slip, and rupture tends to asymmetry.

Pressure profiles are computed with $\frac{\sigma_x}{\sigma_y} = 2.0$ and $d = 200$ m in an impermeable and longitudinal permeable fault. Results are included in panels (**e**) and (**f**) respectively. The selected tectonic ratio and injection distance produce high asymmetric rupture fronts. As in the previous tectonic ratio and distance, the strengthening phenomenon is stronger in longitudinal permeable faults due to the wider pressure bell at the onset of slip, and rupture tends to be even more asymmetrical.

We conclude that longitudinal permeability in faults enhances the strengthening phenomena, promoting asymmetry rupture propagation fronts. Since pressure bells at the onset of slip are wider as faults are more permeable, the strengthening phenomenon is stronger and ruptures tend to be more asymmetrical as faults are more impermeable.

5. Conclusions

Rupture directivity is directly related to the strength of the ground motion and the effects of earthquakes. Both unilateral and bidirectional tectonic earthquakes have been cataloged worldwide, having directivity effects, such as the M7.9 earthquake in Denali, Alaska, 2002, or the M5.1 earthquake in Lorca, Spain, 2011. Diverse studies show that rupture directivity effects may lead to strong pulse-like ground motions [36,93–95]. Likewise, directivity can cause preferential polarization of ground motion in the fault's normal orientation, albeit directivity effects are not equally strong at all periods, fault distances, and orientations with respect to the fault. The potential causes for directivity range from fault properties (geometry, asperity, shape, span, heterogeneity, etc.) to the focus

mechanism features, e.g., size, depth, stress drop, stress state heterogeneity, stress concentrations, and pore pressure distributions, which in turn affect the effective stress state and the proneness to fault instability.

Likewise, directivity effects in injection-induced earthquakes require further research. The model set-up employed in this research included a one-dimensional, homogeneous straight fault embedded in a two-dimensional host rock domain, so no other geometric features have been accounted for. Instead, we have focused on the roles of the distance to the injection well, the confining stress, the fault permeability, the distribution of pore pressure in the hypocenter region, and the undrained response during rupture on the directivity effect. Some combinations of distance and confining stresses result in pronounced asymmetric coseismic rupture propagations, not producing truly unilateral ruptures. Asymmetries are partially explained by the distribution of pore pressure at the onset of the reactivation and the undrained poroelastic response. In our simulations these two factors are controlled by the distance between the injection well and the fault and the ratio of the confining stresses.

On the one hand, the distance between the fault and the injection point determines the pressure distribution along the fault before reactivation. The pressure profile adopts a bell shape. Given that the asymmetry of the rupture increases with the width of the bell shape profile, the asymmetry in the rupture also increases with that distance. On the other hand, the tectonic ratio determines the initial stability of the fault and the required pressure to onset the slip. If low pressure is needed to reactivate the fault, the undrained pressure fronts will predominate over the pressure distribution at the onset of slip, and the rupture will tend to be symmetric. But as the required pressure to reactivate the fault is higher, the undrained effect will promote weakening and strengthening patterns at opposite rupture fronts propagation on the fault that produce asymmetric ruptures.

We study the effect of the longitudinal fault permeability on the rupture asymmetry. The increase in the longitudinal fault permeability leads to wider bell pressure profiles on the fault at the onset of slip. Consequently, the weakening and strengthening patterns during the undrained response are magnified and ruptures are asymmetrical. These poroelastic mechanisms could be applied to analyze cataloged non-symmetric earthquakes, although more research is needed to explore their coupling with the rest of the phenomena proposed in the literature to explain rupture directivity.

The obtained results may help scientists predict the preferred direction of an earthquake depending on the location of the injection point and the rock confinement, and therefore palliate the consequences of earthquakes. This knowledge is useful for underground storage operations in the energy industry, such as deep CO_2 storage, enhanced geothermal systems, or green hydrogen underground storage.

CRediT authorship contribution statement

Sandro Andrés: Writing – review & editing, Writing – original draft, Visualization, Validation, Resources, Methodology, Investigation, Data curation, Conceptualization. **David Santillán:** Writing – review & editing, Writing – original draft, Supervision, Software, Project administration, Investigation, Funding acquisition, Formal analysis, Conceptualization. **Juan Carlos Mosquera:** Writing – review & editing, Validation, Supervision, Resources, Project administration, Methodology. **Luis Cueto-Felgueroso:** Writing – review & editing, Visualization, Validation, Project administration, Funding acquisition, Formal analysis, Conceptualization.

Declaration of competing interest

The authors declare that they have no known competing financial interests or personal relationships that could have appeared to influence the work reported in this paper.

Acknowledgments

This research was supported by the “Ministerio de Ciencia, Innovación y Universidades” and “Agencia Estatal de Investigación” (10.13039/501100011033) and by “ERDF/EU”, through grant HydroPore II (PID2022-137652NB-C43). DSS thanks the financial support of “Comunidad de Madrid” through the call Research Grants for Young Investigators from Universidad Politécnica de Madrid under grant APOYO-JOVENES-21-6YB2DD-127-N6ZTY3, RSIEIH project, research program V PRICIT.

Appendix A. Propagation asymmetry during the rupture

In this appendix, we include the results of pore pressure and symmetry measures during the seismic rupture for simulations with $d = 100$ m and 150 m, and tectonic ratios $\sigma_x/\sigma_y = 2.0$, 2.5, and 2.9. Figs. A.1 and A.2 include results of the pore pressure fronts and symmetry measures for the simulations with $d = 100$ and $d = 150$ m, in the same way as Figs. 7 and 8.

In addition, we include the slip velocity results for all the simulations. In Figs. A.3 and A.4 we observe the same directivity patterns, having an almost symmetric rupture for $d = 50$ m and $\frac{\sigma_x}{\sigma_y} = 2.9$ and the greatest asymmetry for $d = 200$ m and $\frac{\sigma_x}{\sigma_y} = 2.0$. In this case, the slip velocity rupture fronts not only differ in the arrested distance from the hypocenter but also in their magnitude, which increases with the tectonic ratio. The time instants represented in each panel are the same as those of Figs. 7 and A.2, respectively.

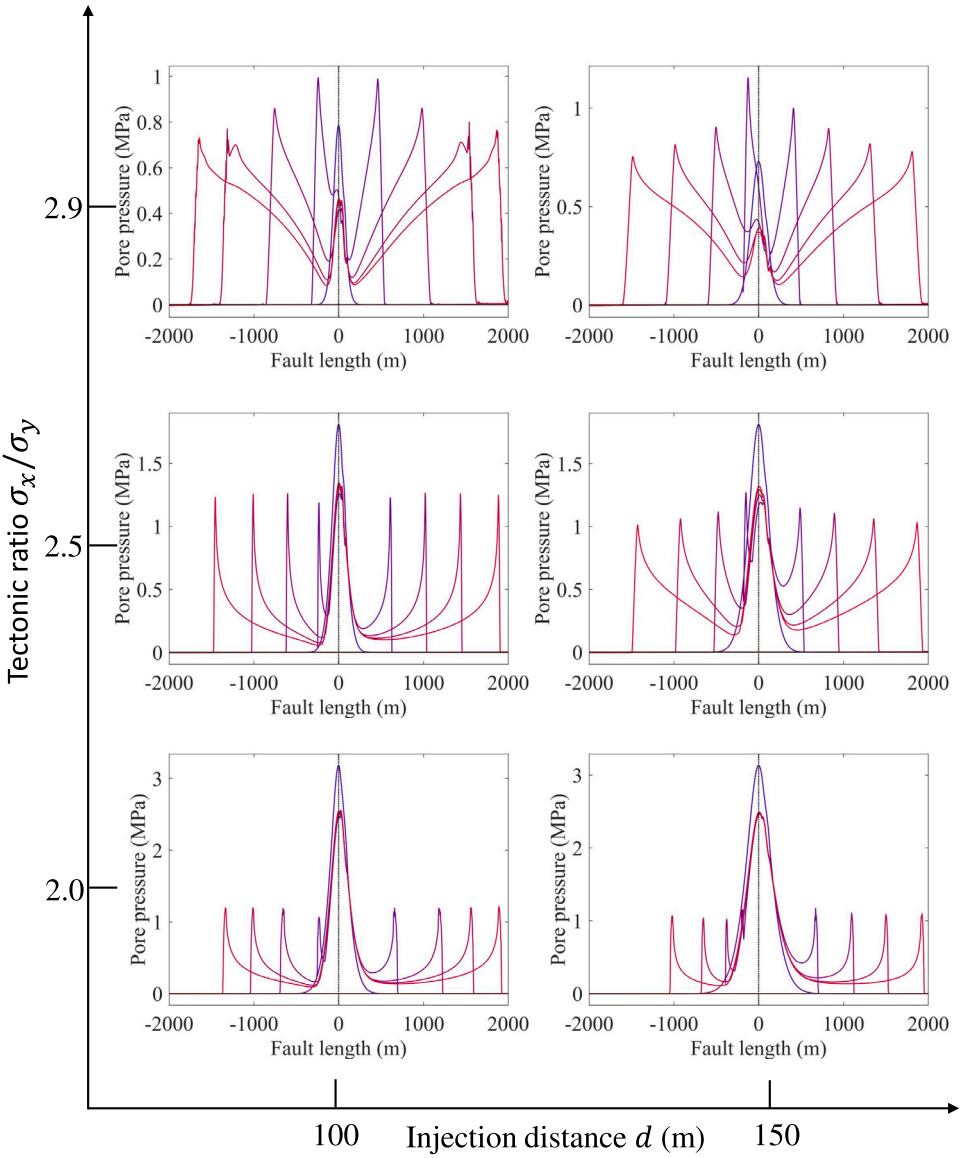

Fig. A.1. Pore pressure distribution along the fault at some instants during the seismic rupture, considering the maximum value between both sides of the fault. Summary of the results for different combinations between tectonic ratio ($\frac{\sigma_x}{\sigma_y}$ = 2.0, 2.5 and 2.9) and distance to the injection well (d = 100 m and 150 m). The slip velocity rupture fronts differ not only in the arrested distance from the hypocenter but also in their magnitude, which increases with the tectonic ratio. The farther the injection well, the more asymmetric the slip velocity profile.

Appendix B. Comparison of quasi-static and dynamic approaches

Our simulations are conducted with a quasi-static approach, Eqs. (1)–(2). To support this choice, we conducted two fully dynamic rupture simulations and compared both results with quasi-static simulations, for d = 50 m and σ_x/σ_y = 2.0; and d = 200 m and σ_x/σ_y = 2.0. Both ruptures are slightly asymmetric. Fig. B.5 shows the results of the two cases computed with both models, i.e., fully dynamic and quasi-static approaches. Although there are some differences, the global behavior and the degree of symmetry of the rupture are almost the same, as seen in panels (**a**) and (**b**) for the case with d = 200 m and σ_x/σ_y = 2.0. Panels (**c**) and (**d**) show the superposition of the quasi-static and dynamic results for the cases. Although slight discrepancies between both approaches arise, the pressure distribution at the fault reactivation time and the advance of the undrained pressure fronts are quite similar.

Data availability

No data was used for the research described in the article.

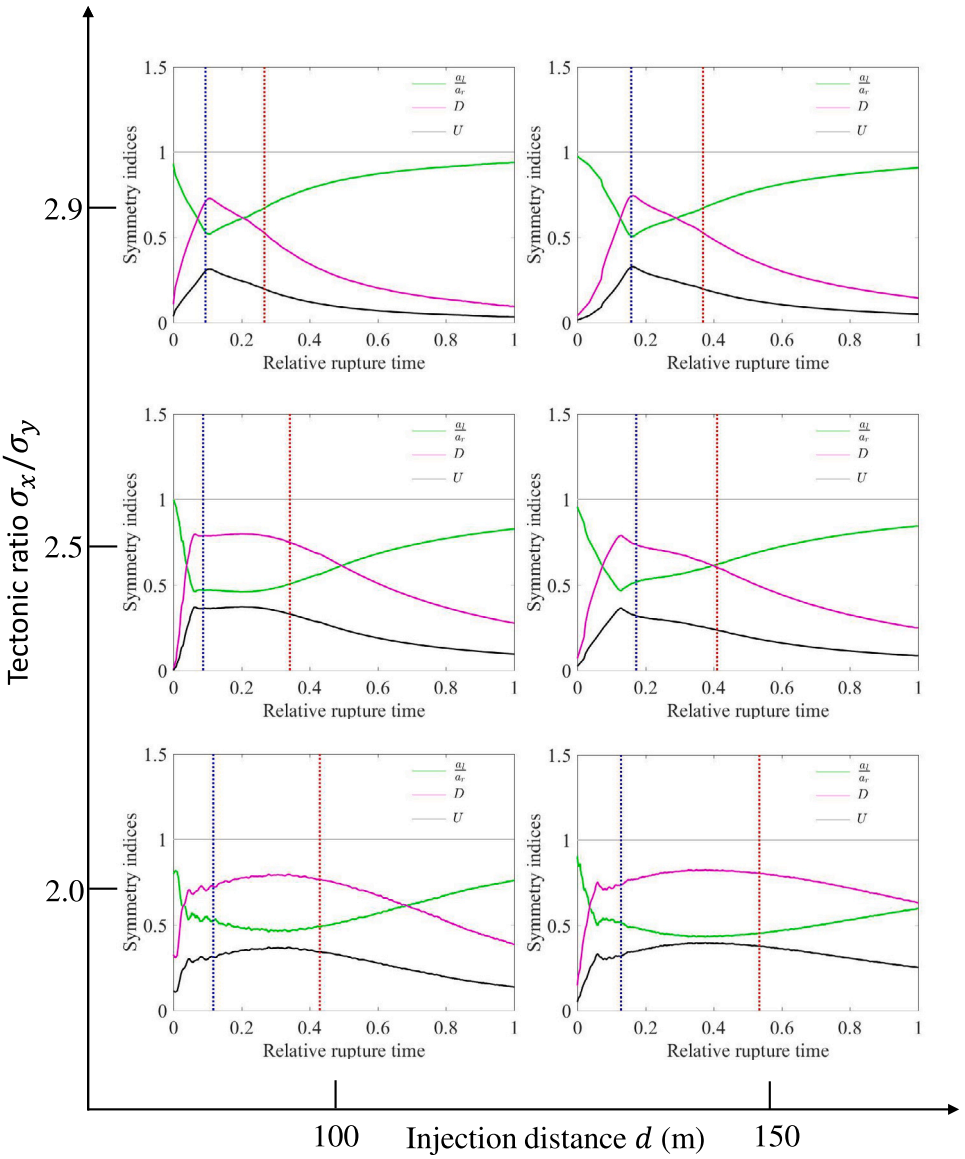

Fig. A.2. Evolution of proportion unilateral rupture U and directivity ratio D during the rupture propagation. Summary of the results for different combinations between tectonic ratio ($\frac{\sigma_x}{\sigma_y}$ = 2.0, 2.5 and 2.9) and distance to the injection well (d = 100 m and 150 m). The blue and red lines represent the moment when the right and left rupture fronts surpass the reactivation pressure bell, respectively.

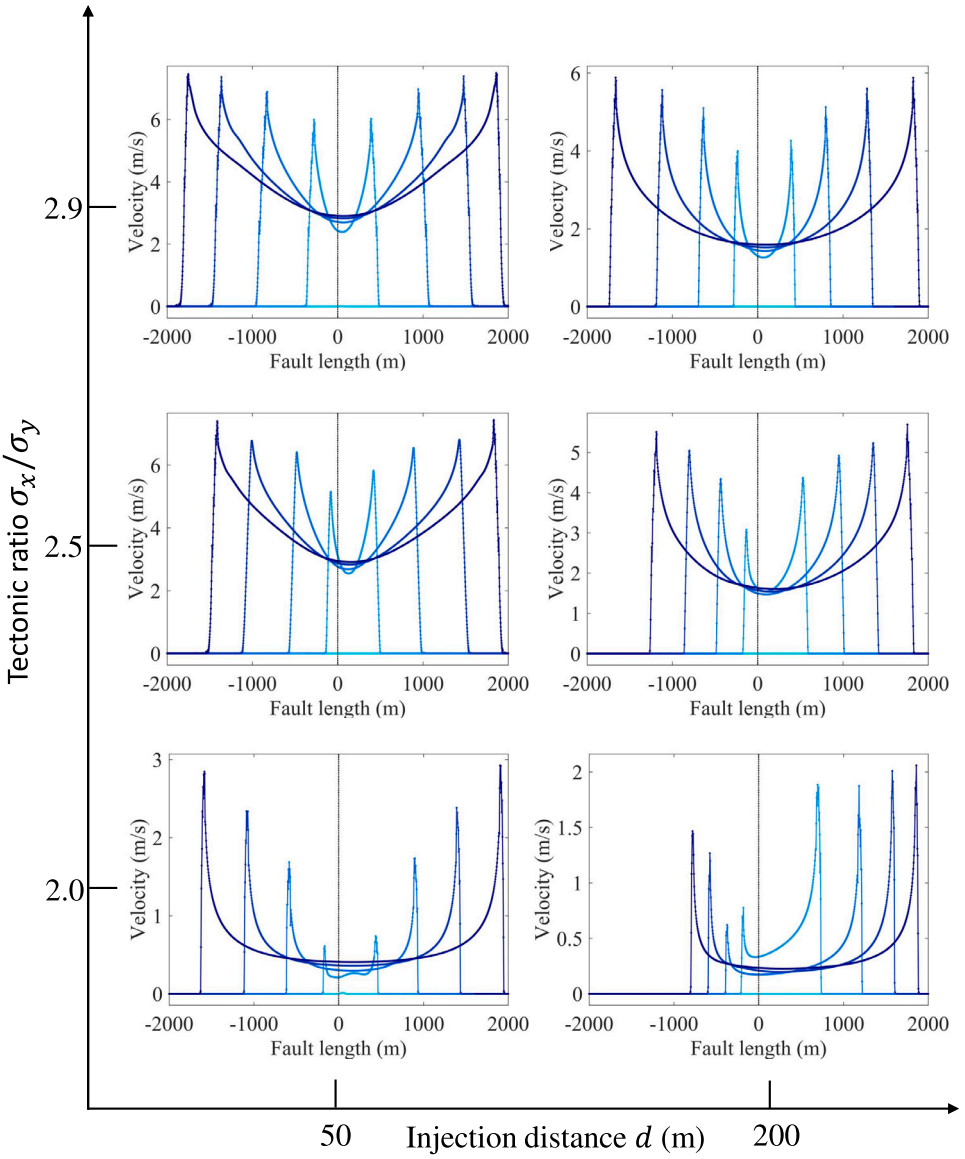

Fig. A.3. Slip velocity distribution along the fault during the seismic rupture. Summary of the results for various combinations between tectonic ratio ($\frac{\sigma_x}{\sigma_y} = 2.0$, 2.5 and 2.9) and distance to the injection well ($d = 50$ m and 200 m). The slip velocity rupture fronts differ not only in the arrested distance from the hypocenter but also in their magnitude, which increases with the tectonic ratio. The farther the injection well the more asymmetric the slip velocity profile. The rupture instants represented are the same as those of Fig. 7.

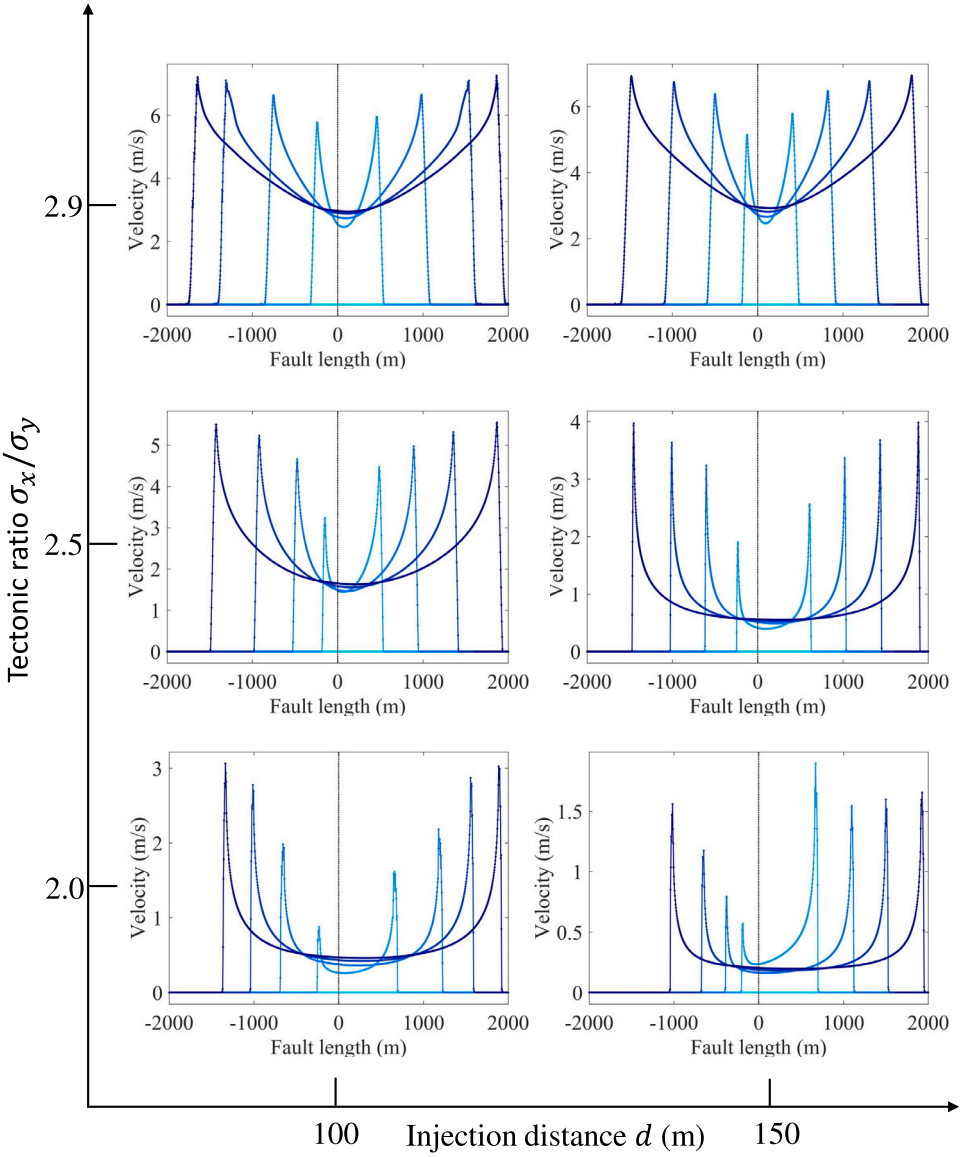

Fig. A.4. Slip velocity distribution along the fault during the seismic rupture. Summary of the results for various combinations between tectonic ratio ($\frac{\sigma_x}{\sigma_y}$ = 2.0, 2.5 and 2.9) and distance to the injection well (d = 100 m and 150 m). The rupture time steps represented in each panel are the same as those of Fig. A.1.

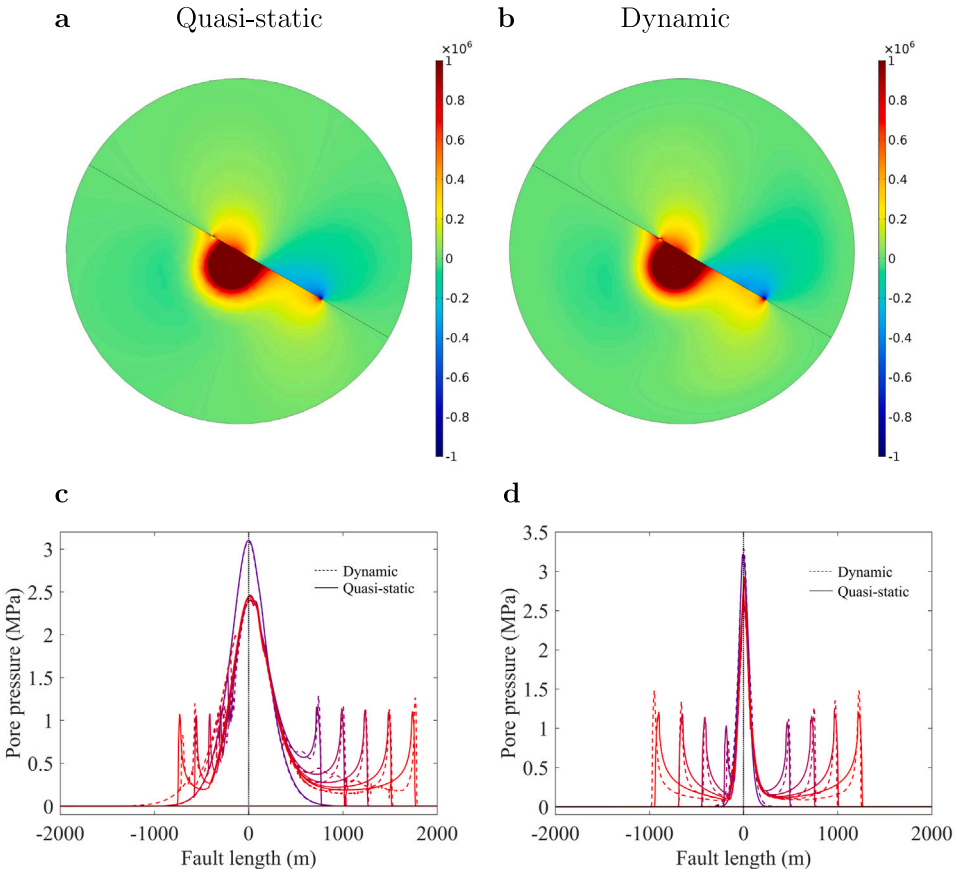

Fig. B.5. Results from quasi-static (left) and dynamic (right) simulations. Panels (**a**) and (**b**) show the pore pressure fields for $d = 200$ m $\sigma_x/\sigma_y = 2.0$. Both fields are quite similar at equivalent instants during the rupture propagation. Panels (**c**) and (**d**) depict the change in pore pressure along the fault analogously to Fig. 7, for $d = 200$ m and $\sigma_x/\sigma_y = 2.0$, and $d = 50$ m and $\sigma_x/\sigma_y = 2.0$, respectively. Quasi-static results are plotted with solid lines and dynamic results with dashed lines.

References

[1] National Research Council. Induced seismicity potential in energy technologies. Washington, DC: National Academies Press; 2013.
[2] Ellsworth WL. Injection-induced earthquakes. Science 2013;341:1225942.
[3] Walsh FR, Zoback MD. Oklahoma's recent earthquakes and saltwater disposal. Sci Adv 2015;1:e1500195.
[4] Van Eck T, Goutbeek F, Haak H, Dost B. Seismic hazard due to small-magnitude, shallow-source, induced earthquakes in the netherlands. Eng Geol 2006;87:105–21.
[5] Deichmann N, Giardini D. Earthquakes induced by the stimulation of an enhanced geothermal system below Basel (Switzerland). Seismol Res Lett 2009;80:784–98.
[6] Grünthal G. Induced seismicity related to geothermal projects versus natural tectonic earthquakes and other types of induced seismic events in Central Europe. Geothermics 2014;52:22–35.
[7] Mahani AB, Schultz R, Kao H, Walker D, Johnson J, Salas C. Fluid injection and seismic activity in the northern Montney play. British Columbia, Canada, with special reference to the 17 August 2015 Mw 4.6 induced earthquake. Bull Seismol Soc Am 2017;107:542–52.
[8] Lei X, Huang D, Su J, Jiang G, Wang X, Wang H, Guo X, Fu H. Fault reactivation and earthquakes with magnitudes of up to Mw4.7 induced by shale-gas hydraulic fracturing in Sichuan Basin, China. Sci Rep 2017;7:1–12.
[9] Foulger GR, Wilson MP, Gluyas JG, Julian BR, Davies RJ. Global review of human-induced earthquakes. Earth-Sci Rev 2018;178:438–514.
[10] Horton S. Disposal of hydrofracking waste fluid by injection into subsurface aquifers triggers earthquake swarm in central Arkansas with potential for damaging earthquake. Seismol Res Lett 2012;83:250–60.
[11] Shirzaei M, Ellsworth WL, Tiampo KF, González PJ, Manga M. Surface uplift and time-dependent seismic hazard due to fluid injection in eastern Texas. Science 2016;353:1416–9.
[12] Keranen KM, Weingarten M, Abers GA, Bekins BA, Ge S. Sharp increase in central Oklahoma seismicity since 2008 induced by massive wastewater injection. Science 2014;345:448–51.
[13] Weingarten M, Ge S, Godt JW, Bekins BA, Rubinstein JL. High-rate injection is associated with the increase in us mid-continent seismicity. Science 2015;348:1336–40.
[14] Deng K, Liu Y, Harrington RM. Poroelastic stress triggering of the december 2013 crooked lake. Alberta, induced seismicity sequence. Geophys Res Lett 2016;43:8482–91.
[15] Clarke H, Eisner L, Styles P, Turner P. Felt seismicity associated with shale gas hydraulic fracturing: The first documented example in Europe. Geophys Res Lett 2014;41:8308–14.

[16] Santillán D, Juanes R, Cueto-Felgueroso L. Phase field model of fluid-driven fracture in elastic media: Immersed-fracture formulation and validation with analytical solutions. J Geophys Res Solid Earth 2017a;122:2565–89.
[17] Santillán D, Mosquera JC, Cueto-Felgueroso L. Fluid-driven fracture propagation in heterogeneous media: Probability distributions of fracture trajectories. Phys Rev E 2017b;96:053002.
[18] Santillán D, Juanes R, Cueto-Felgueroso L. Phase field model of hydraulic fracturing in poroelastic media: Fracture propagation, arrest, and branching under fluid injection and extraction. J Geophys Res Solid Earth 2018;123:2127–55.
[19] Brodsky EE, Lajoie LJ. Anthropogenic seismicity rates and operational parameters at the Salton Sea Geothermal Field. Science 2013;341:543–6.
[20] Andrés S, Santillán D, Mosquera JC, Cueto-Felgueroso L. Hydraulic stimulation of geothermal reservoirs: Numerical simulation of induced seismicity and thermal decline. Water 2022;14.
[21] White JA, Foxall W. Assessing induced seismicity risk at CO2 storage projects: Recent progress and remaining challenges. Int J Greenh Gas Control 2016;49:413–24.
[22] Zoback MD, Gorelick SM. Earthquake triggering and large–scale geologic storage of carbon dioxide. Proc Natl Acad Sci USA 2012;109:10164–8.
[23] Pampillón P, Santillán D, Mosquera JC, Cueto-Felgueroso L. Geomechanical constraints on hydro-seismicity: Tidal forcing and reservoir operation. Water 2020;12.
[24] Keranen KM, Savage HM, Abers GA, Cochran ES. Potentially induced earthquakes in Oklahoma, USA: Links between wastewater injection and the 2011 Mw 5.7 earthquake sequence. Geology 2013;41:699–702.
[25] McGarr A. Maximum magnitude earthquakes induced by fluid injection. J Geophys Res Solid Earth 2014;119:1008–19.
[26] Olson EL, Allen RM. The deterministic nature of earthquake rupture. Nature 2005;438(212).
[27] Gischig V. Rupture propagation behavior and the largest possible earthquake induced by fluid injection into deep reservoirs. Geophys Res Lett 2015;42:7420–8.
[28] Dempsey D, Suckale J. Collective properties of injection-induced earthquake sequences: 1. Model description and directivity bias. J Geophys Res Solid Earth 2016;121:3609–37.
[29] Lengliné O, Got JL. Rupture directivity of microearthquake sequences near Parkfield, California. Geophys Res Lett 2011;38.
[30] McGuire J, Zhao L, T.H. J. Predominance of unilateral rupture for a global catalog of large earthquakes. Bull Seismol Soc Am 2002;92:3309–17.
[31] Calderoni G, Rovelli A, Ben-Zion Y, Giovambattista RDi. Along-strike rupture directivity of earthquakes of the 2009 L'Aquila, central Italy, seismic sequence. Geophys J Int 2015;203:399–415.
[32] Kane D, Shearer P, Goertz-Allmann B, Vernon F. Rupture directivity of small earthquakes at parkfield. J Geophys Res Solid Earth 2013;118:212–21.
[33] Boatwright J. The persistence of directivity in small earthquakes. Bull Seismol Soc Am 2007;97:1850–61.
[34] Király-Proag E, Satriano C, Bernard P, Wiemer S. Rupture process of the Mw 3.3 earthquake in the St. Gallen 2013 geothermal reservoir, Switzerland. Geophys Res Lett 2019;46:7990–9.
[35] Folesky J, Kummerow J, Shapiro S, Häring H, Asanuma H. Rupture directivity of fluid-induced microseismic events: Observations from an enhanced geothermal system. J Geophys Res Solid Earth 2016;121:8034–47.
[36] Somerville PG. Magnitude scaling of the near fault rupture directivity pulse. Phys Earth Planet Inter 2003;137:201–12.
[37] Dunham EM, Favreau P, Carlson J. A supershear transition mechanism for cracks. Science 2003;299:1557–9.
[38] Andrews DJ, Ben-Zion Y. Wrinkle-like slip pulse on a fault between different materials. J Geophys Res Solid Earth 1997;102:553–71.
[39] Ben-Zion Y. Dynamic ruptures in recent models of earthquake faults. J Mech Phys Solids 2001;49:2209–44.
[40] Shi Z, Ben-Zion Y. Dynamic rupture on a bimaterial interface governed by slip-weakening friction. Geophys J Int 2006;165:469–84.
[41] Rudnicki J, Rice J. Effective normal stress alteration due to pore pressure changes induced by dynamic slip propagation on a plane between dissimilar materials. J Geophys Res 2006;111(B10308).
[42] Brener E, Weikamp M, Spatschek R, Bar-Sinai Y, Bouchbinder E. Dynamic instabilities of frictional sliding at a bimaterial interface. J Mech Phys Solids 2016;89:149–73.
[43] Langer S, Weatherley D, Olsen-Kettle L, Finzi Y. Stress heterogeneities in earthquake rupture experiments with material contrasts. J Mech Phys Solids 2013;61:742–61.
[44] Dunham E, Rice J. Earthquake slip between dissimilar poroelastic materials. J Geophys Res 2008;113(B09304).
[45] Harris R, Day S. Material contrast does not predict earthquake rupture propagation direction. Geophys Res Lett 2005;32(L23301).
[46] Biot MA. General theory of three-dimensional consolidation. J Appl Phys 1941;12:155–64.
[47] Rice JR, Cleary MP. Some basic stress diffusion solutions for fluid-saturated elastic porous media with compressible constituents. Rev Geophys Space Phys 1976;14:227–41.
[48] Rice JR. Constitutive relations for fault slip and earthquake instabilities. Pure Appl Geophys 1983;121:443–75.
[49] Ruina A. Slip instability and state variable friction laws. J Geophys Res 1983;88:10359–70.
[50] Cueto-Felgueroso L, Santillán D, Mosquera JC. Stick–slip dynamics of flow-induced seismicity on rate and state faults. Geophys Res Lett 2017;44:4098–106.
[51] Cueto-Felgueroso L, Vila C, Santillan D, Mosquera JC. Numerical modeling of injection–induced earthquakes using laboratory–derived friction laws. Water Resour Res 2018;54:1–27.
[52] Pampillón P, Santillán D, Mosquera JC, Cueto-Felgueroso L. The role of pore fluids in supershear earthquake ruptures. Sci Rep 2023;13.
[53] Andrés S, Dentz M, Cueto-Felgueroso L. Multirate mass transfer approach for double-porosity poroelasticity in fractured media. Water Resour Res 2021;57:e2021WR029804.
[54] Segura JM, Carol I. Coupled HM analysis using zero-thickness interface elements with double nodes. Part I: Theoretical model. Int J Numer Anal Methods Geomech 2008;32:2083–101.
[55] Jha B, Juanes R. Coupled multiphase flow and poromechanics: A computational model of pore pressure effects on fault slip and earthquake triggering. Water Resour Res 2014;50:3776–808.
[56] Bowden FP, Tabor D. The friction and lubrication of solids I. London, UK: Clarendon Press; 1950.
[57] Baumberger T, Caroli C. Solid friction from stick–slip down to pinning and aging. Adv Phys 2006;55:279–348.
[58] Barber JR. Multiscale surfaces and Amontons' law of friction. Tribol Lett 2013;49:539–43.
[59] Pampillón P, Santillán D, Mosquera JC, Cueto-Felgueroso L. Dynamic and quasi–dynamic modeling of injection–induced earthquakes in poroelastic media. J Geophys Res Solid Earth 2018;123:5730–59.
[60] Yang Z, Juanes R. Two sides of a fault: Grain-scale analysis of pore pressure control on fault slip. Phys Rev E 2018;97:022906.
[61] Heimisson ER, Dunham EM, Almquist M. Poroelastic effects destabilize mildly rate-strengthening friction to generate stable slow slip pulses. J Mech Phys Solids 2019;130:262–79.
[62] Rabinowicz E. The nature of the static and kinetic coefficients of friction. J Appl Phys 1951;22:1373–9.
[63] Baumberger T, Berthoud P, Caroli C. Physical analysis of the state- and rate-dependent friction law. II. Dynamic friction. Phys Rev B 1999;60:3928–39.
[64] Berthoud P, Baumberger T, G'Sell C, Hiver JM. Physical analysis of the state- and rate-dependent friction law: Static friction. Phys Rev B 1999;59:14313–27.
[65] Putelat T, Dawes JHP. Steady and transient sliding under rate-and-state friction. J Mech Phys Solids 2015;78:70–93.
[66] Scuderi MM, Collettini C, Marone C. Frictional stability and earthquake triggering during fluid pressure stimulation of an experimental fault. Earth Planet Sci Lett 2017;477:84–96.
[67] Scuderi MM, Collettini C. Fluid–injection and the mechanics of frictional stability of shale–bearing faults. J Geophys Res Solid Earth 2018;123:8364–84.

[68] Yang Z, Zhang HP, Marder M. Dynamics of static friction between steel and silicon. Proc Natl Acad Sci USA 2008;105:13264–8.
[69] Dieterich JH. Modeling of rock friction: 1. Experimental results and constitutive equations. J Geophys Res 1979;84:2161–8.
[70] Dieterich JH. Time-dependent friction and the mechanics of stick–slip. Pure Appl Geophys 1978;116:790–806.
[71] Rice JR, Ruina A. Stability of steady frictional slipping. J Appl Mech 1983;50:343–9.
[72] Gu JC, Rice JR, Ruina AL, Simon TT. Slip motion and stability of a single degree of freedom elastic system with rate and state dependent friction. J Mech Phys Solids 1984;32:167–96.
[73] Andrés S, Santillán D, Mosquera J, Cueto-Felgueroso L. Delayed weakening and reactivation of rate-and-state faults driven by pressure changes due to fluid injection. J Geophys Res Solid Earth 2019;124:11917–37.
[74] Beeler N, Tullis T, Blanpied M, Weeks J. Frictional behavior of large displacement experimental faults. J Geophys Res Solid Earth 1996;101:8697–715.
[75] COMSOL. COMSOL multiphysics structural mechanics module user's guide v5.2a. Stockholm, Sweden: Comsol; 2016.
[76] Hindmarsh AC, Brown PN, Grant KE, Lee SL, Serban R, Shumaker DE, Woodward CS. SUNDIALS: Suite of nonlinear and differential/algebraic equation solvers. ACM Trans Math Software 2005;31:363–96.
[77] Segall P. Stress and subsidence resulting from subsurface fluid withdrawal in the epicentral region of the 1983 Coalinga earthquake. J Geophys Res Solid Earth 1985;90:6801–16.
[78] Segall P. Induced stresses due to fluid extraction from axisymmetric reservoirs. Pure Appl Geophys 1992;139:535–60.
[79] Segall P, Fitzgerald SD. A note on induced stress changes in hydrocarbon and geothermal reservoirs. Tectonophysics 1998;289:117–28.
[80] Soltanzadeh H, Hawkes CD. Semi-analytical models for stress change and fault reactivation induced by reservoir production and injection. J Pet Sci Eng 2008;60:71–85.
[81] Soltanzadeh H, Hawkes CD. Assessing fault reactivation tendency within and surrounding porous reservoirs during fluid production or injection. Int J Rock Mech Min Sci 2009;46:1–7.
[82] Wang L, Bai B, Li X, Liu M, Wu H, Hu S. An analytical model for assessing stability of pre-existing faults in caprock caused by fluid injection and extraction in a reservoir. Rock Mech Rock Eng 2016;49:2845–63.
[83] Jansen JD, Singhal P, Vossepoel FC. Insights from closed-form expressions for injection-and production-induced stresses in displaced faults. J Geophys Res Solid Earth 2019;124:7193–212.
[84] Wu H, Vilarrasa V, De Simone S, Saaltink M, Parisio F. Analytical solution to assess the induced seismicity potential of faults in pressurized and depleted reservoirs. J Geophys Res Solid Earth 2021;126:e2020JB020436.
[85] Wu H, Rutqvist J, Vilarrasa V. Analytical solution to quickly assess ground displacement for a pressurized or depleted deep reservoir intersected by a fault in a half space. Int J Rock Mech Min Sci 2024;174:105641.
[86] Barry SI, Mercer GN. Exact solutions for two-dimensional time-dependent flow and deformation within a poroelastic medium. J Appl Mech 1999;66:536–40.
[87] Sáez A, Lecampion B, Bhattacharya P, Viesca RC. Three-dimensional fluid-driven stable frictional ruptures. J Mech Phys Solids 2022;160:104754.
[88] Sáez A, Lecampion B. Fluid-driven slow slip and earthquake nucleation on a slip-weakening circular fault. J Mech Phys Solids 2024;183:105506.
[89] Carslaw H, Jaeger J. Conduction of heat in solids. Oxford, UK: Oxford University Press; 1989.
[90] Molina O, Vilarrasa V, Zeidouni M. Geologic carbon storage for shale gas recovery. Energy Procedia 2017;114:5748–60.
[91] Ampuero JP, Rubin AM. Earthquake nucleation on rate and state faults – Aging and slip laws. J Geophys Res Solid Earth 2008;113.
[92] Buckingham E, Buckingham E. On physically similar systems; illustrations of the use of dimensional equations. Phys Rev 1914;4:345–76.
[93] Bertero VV, Mahin SA, Herrera RA. Aseismic design implications of near-fault San Fernando earthquake records. Earthq Eng Struct D 1978;6:31–42.
[94] Anderson JC, Bertero VV. Uncertainties in establishing design earthquakes. J Struct Eng 1987;113:1709–24.
[95] Gordo-Monsó C, Miranda E. Significance of directivity effects during the 2011 Lorca earthquake in Spain. Bull Earthq Eng 2018;16:2711–28.